Review Article

Interband Quantum Cascade Infrared Photodetectors: Current Status and Future Trends

P. Martyniuk,[1,2,*] A. Rogalski,[1] and S. Krishna[2]

[1] *Institute of Applied Physics, Military University of Technology, 2 Kaliskiego Str., 00-908 Warsaw, Poland*
[2] *Department of Electric Engineering, The Ohio State University, 2024 Neil Avenue, Columbus, Ohio 43210, USA*

(Received 28 July 2021; accepted 8 December 2021; published 11 February 2022)

One of the critical limitations of photonic infrared (IR) photodetectors is the cooling requirement that is placed on it. Uncooled detectors are usually based on thermal detectors. Currently, microbolometer thermal detectors are produced in a larger volume than those of all other IR array technologies together. In recent years, their cost has drastically dropped (about 15% per year). Although their performance is modest, thermal detectors suffer from slow responses and they are not useful in multispectral detection. The (Hg, Cd)Te ternary system dominates photonic IR detector technology. It also has a superior performance under high operating temperature (HOT) conditions. At present, technological efforts are directed towards advanced heterojunction photovoltaic (Hg, Cd)Te detectors. In the last decade, several concepts have been proposed to improve the HOT photon detector's performance to include various kinds of materials, such as type-II $A^{III}B^{V}$ superlattices (T2SLs), two-dimensional materials, and colloidal quantum dots. Among them, the most promising are interband quantum cascade photodetectors (IB QCPs) based on $A^{III}B^{V}$ T2SLs considered in this paper. This paper reviews the history, present status, and possible future developments of IB QCPs for IR HOT applications. To date, the "Rule 07" metric has been used as a proper approach for the prediction of the photodiode performance of *p*-on-*n* (Hg, Cd)Te and as a reference benchmark for alternative technologies. However, recently, it has been shown [Lee *et al.*, Proc. SPIE 11407, 114070X (2020)] that uncooled depletion-limited (Hg, Cd)Te photodiodes exhibit further performance enhancement called "Law 19," which is background-limited detectivity in the long-wavelength infrared spectral range. In this context, here, the performance of IB QCPs is compared with Law 19.

DOI: 10.1103/PhysRevApplied.17.027001

I. INTRODUCTION

Looking back into the history of infrared (IR) radiation it can be observed that all physical effects in the range of about 0.1–1 eV are proposed for IR photodetectors. Figure 1 shows a timeline of IR detectors and imaging systems that have been developed to date. The following effects can be enumerated: thermoelectric (thermopile), change in electric resistivity (bolometers), gas expansion (Golay cell), pyroelectricity (pyroelectric detectors), photon drag, photoemission (PtSi Schottky barriers), fundamental absorption (intrinsic photodetectors), impurity absorption (extrinsic photodetectors), low-dimensional solids [quantum well (QW), superlattices (SLs), and quantum dot (QD) detectors], two-dimensional (2D) materials, and colloidal quantum dots (CQDs).

The fundamental optical excitation processes in semiconductors are illustrated in Fig. 2 [1]. In the bulk material, the basic excitation mechanism is connected to band-to-band electron transitions or carrier transitions from the doping level to the conduction (CB) or valence band (VB). In the QWs [Fig. 2(b)] the intersubband (IS) absorption occurs between the discrete energy levels of the QW associated with the CB (*n* doped) or VB (*p* doped). As is shown, the QW consists of a thin (below 10 nm) low-band-gap material sandwiched between two large-band-gap-barrier materials. The quantized levels in the CB and VB are created by the low-dimensional effect, depending mainly on the QW thickness and the well potential. In the case of the type-II InAs/GaSb superlattice (T2SL) [Fig. 2(c)], the SL band gap is determined by the energy difference between the electron miniband (E_1) and the first heavy-hole state (HH_1) at the Brillouin-zone center. A consequence of the type-II band alignment is the spatial separation of electrons and holes. Such low-dimensional electron systems, including QWs, SLs, and QDs, fabricated mainly by molecular beam epitaxy (MBE), result in the incredibly diverse number of IR photodetectors that are currently known.

Since the discovery of graphene in 2004, its applications in photonic devices have been intensively investigated. The extraordinary and unusual electronic and optical

*piotr.martyniuk@wat.edu.pl

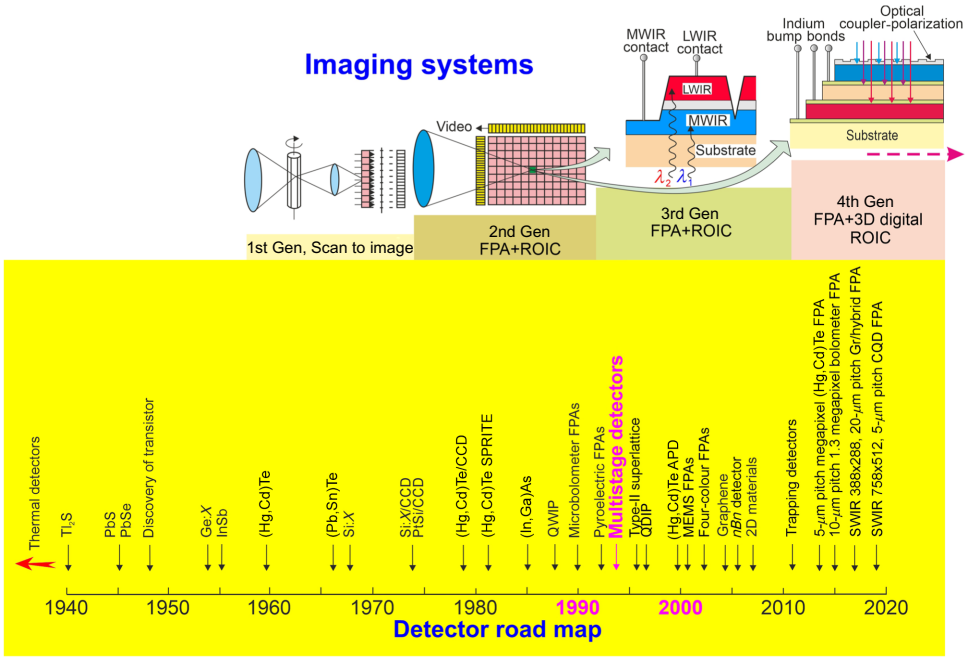

FIG. 1. History of IR detectors. Four generations of systems for both civilian and military applications: first generation (scanning systems), second generation (staring systems, electronically scanned), third generation (staring systems with a large number of pixels and two-color functionality), and fourth generation [staring systems with very large number of pixels, multicolor functionality, 3D read-out integrated circuit (ROIC), and other on-chip functions; e.g., better radiation and pixel coupling, avalanche multiplication in pixels, polarization or phase sensitivity].

properties allow graphene and other 2D materials to be promising candidates for IR photodetectors. To date, however, their position in the wider IR detector family is considered to be marginal [2].

II. MULTISTAGE PHOTODETECTORS

Initial efforts to develop high-operating-temperature (HOT) photodetectors in the 1970s and 1980s concentrated on (Hg, Cd)Te photoconductors and photoelectromagnetic detectors [3,4]. At the end of the 20th century, technological efforts were directed to advanced heterojunction photovoltaic (Hg, Cd)Te detectors. It is well known, however, that in a conventional photodiode the responsivity (R_i) and diffusion length (L) are closely coupled, and an increase in the absorber thickness much beyond the diffusion length may not result in the desired improvement in the signal-to-noise (S/N) ratio. This effect is particularly pronounced at high temperatures, where diffusion lengths are typically reduced. For example, for (Hg, Cd)Te photodiodes operating in the long-wavelength IR (LWIR) spectral range, the absorption depth is longer than the diffusion length and, therefore, only a limited fraction of photogenerated charges contribute to the quantum efficiency (QE).

A. Multistage (Hg, Cd)Te heterojunction photodiodes

To increase the voltage responsivity, an efficient improvement was proposed by Piotrowski and Gawron in 1995 through the fabrication of a multiple-heterojunction photovoltaic device [5]. The multiheterojunction device consists of a structure based on backside-illuminated n^+-p-P photodiodes (symbol "+" denotes heavy doping; capital letter denotes a wider gap), as shown in Fig. 3. The p-type 3-μm-thick doping levels about 10^{16} cm^{-3} active layers are grown on GaAs substrates using metal-organic chemical vapor deposition (CVD) or liquid-phase epitaxial (LPE) techniques and *in situ* As (Sb) doping. The trenches in the epilayer are delineated by wet chemical etching using Br-ethylene glycol or Br-HBr solutions. The sample is placed at about 45° to the direction of the Ar^+ beam using a Kaufman-type ion gun, so only one wall of the trench

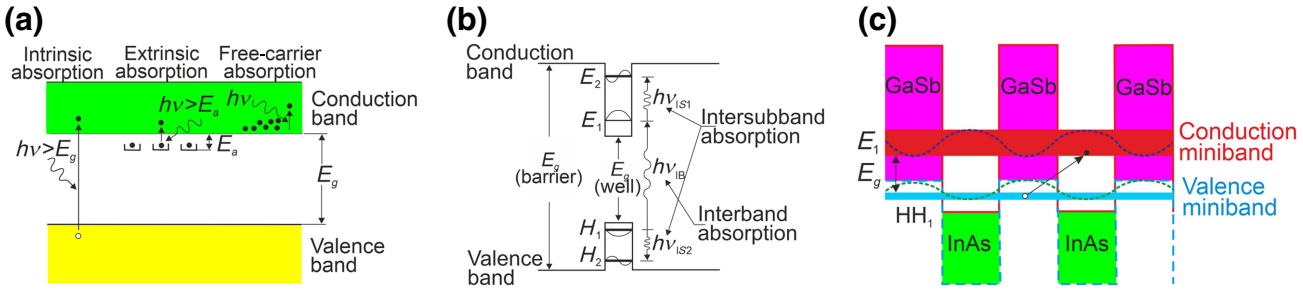

FIG. 2. Optical excitation mechanisms in (a) bulk semiconductors, (b) QWs, and (c) InAs/GaSb T2SLs (based on Ref. [1]).

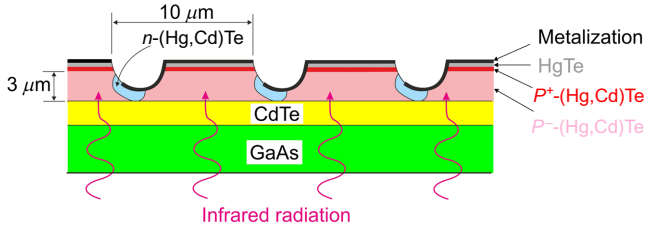

FIG. 3. Backside-illuminated multiple heterojunction device (based on Ref. [5]).

is exposed to the beam, which results in n-type conversion. As shown in Fig. 3, the multiheterojunction device is constructed from backside-illuminated n^+-p-P photodiodes connected in series. The advantages of such a design are a large voltage responsivity and a short response time, but, on the other hand, the device's response depends on the polarization of incident radiation and is nonuniform across the active area.

In the multiple (Hg, Cd)Te heterojunction shown in Fig. 3, the junction's planes are perpendicular to the surface. This design is not useful for detector-array fabrication and scaling processes. A more promising design is stacked tunnel junctions connected in series, as shown in Fig. 4(a). This idea is similar to multijunction solar cells. Potentially, this device is capable of reaching a high QE, a large differential resistance, and a fast response. As shown, each cell consists of a lightly p-type-doped absorber and wide-band gap heavily doped N^+ and P^+ contact layers. The heterojunction contacts collect photogenerated charge carriers absorbed in every absorber. However, an issue is the resistance of adjacent N^+ and P^+ regions.

Figure 4(b) shows the detector performance versus number of cells based on the N^+-p-P^+ structure with 1-μm-thick absorbers. The series connection of cells allows the device resistance and voltage responsivity to be increased. It appears that the detectivity (D^*) initially increases versus the number of cells, reaching a maximum for $N = 15$ stages. For a larger number of cells, assuming Johnson thermal-noise dependence, detectivity tends to saturate or decrease. For practical reasons, the number of cells can be reduced to about 10; then the detectivity is about 2 times larger in comparison to that of a single-cell device. However, the main practical problem in the fabrication of stacked heterojunctions is the relatively large resistance of adjacent N^+ and P^+ regions.

B. Intersubband quantum cascade photodetectors

To avoid the limitation imposed by the reduced diffusion length and effectively increase the absorption efficiency of standard photodiodes, the detector designs, called IS quantum cascade photodetectors (QCPs), were introduced

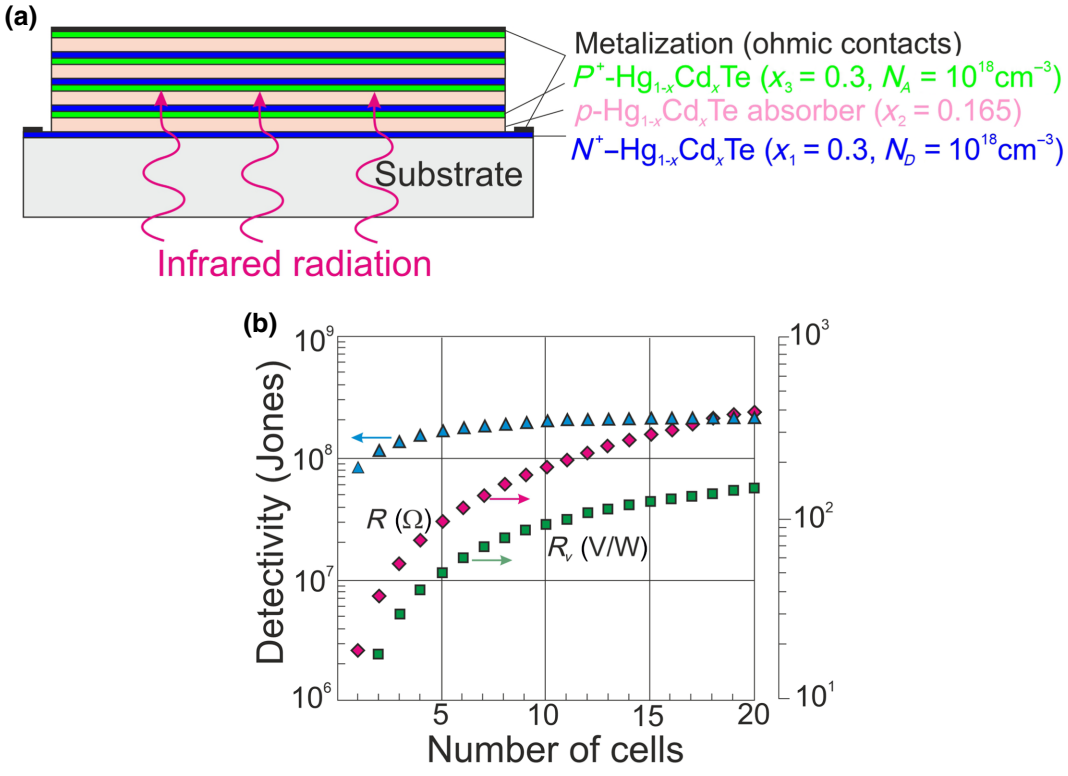

FIG. 4. Multiple (Hg, Cd)Te heterojunction photovoltaic device: (a) four-cell stacked multiple detector, (b) detector performance versus number of cells (based on Ref. [5]).

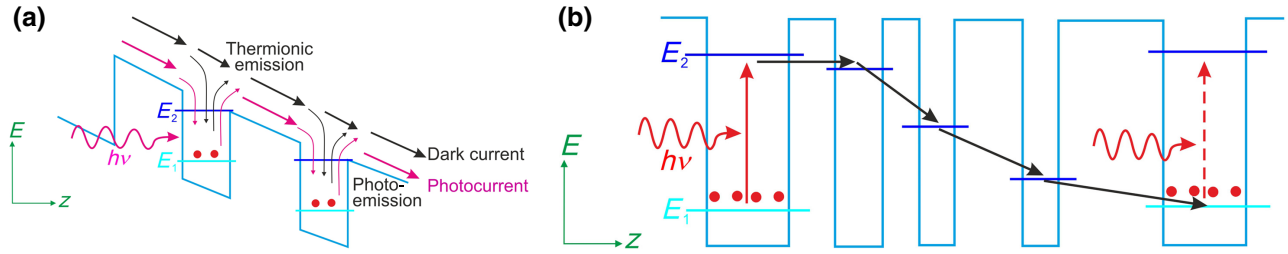

FIG. 5. QWIP (a) and IS QCP (b) conduction-band diagram. In the QWIP, electron transport is accomplished by an external voltage, whereas in the IS QCP an internal potential ramp ensures carrier transport (photovoltaic effect).

in the early 2000s based on quantum-well infrared photodetectors (QWIPs) and quantum cascade lasers (QCLs) [6–9]. A distinguishing feature of both types of photodetectors is that intraband processes can be implemented in chemically stable wide-band-gap materials. The development of these devices is possible due to the powerful MBE growth technique. Most IS transition devices are based on $A^{III}B^{V}$ GaAs [GaAs QWs with (Al,Ga)As barriers lattice-matched to GaAs] and InP [(In,Ga)As QWs with barriers of (Al, In)As lattice-matched to InP] material systems.

The concept of using IR photoexcitation from QWs was suggested by Smith *et al.* [10]. Coon and Karunasiri made a similar suggestion and pointed out that the optimum response should occur when the first excited state lies near the classical threshold for photoemission from the QW [11]. A key future development of these early concepts involved recognizing that intraband transitions would permit the use of wide-gap-material systems, such as (Al,Ga)As, with fewer material problems than those of (Hg, Cd)Te. West and Eglash demonstrated large IS absorption between confined states in 50-GaAs QWs [12]. In 1987, Levine and co-workers fabricated a QWIP operating at 10 μm [13]. It appears that transitions between the ground state and the first excited state have relatively large oscillator strengths and absorption coefficient (α).

A key result of the photovoltaic QWIP structure is the application of an internal electric field. This idea extends back to 1997 when the four-zone QWIP was developed [14]. Lowering of the dark current and suppression of the generation-recombination (g-r) noise is expected because these devices, in principle, operate without external bias. However, their photocurrent is associated with a much smaller gain in comparison with that of photoconductive QWIPs.

A structure similar to that of an IS QCP (without calling it so) was demonstrated in 2002 by Hofstetter *et al.* [8] The QCP name was introduced by Gendron *et al.* as recently as

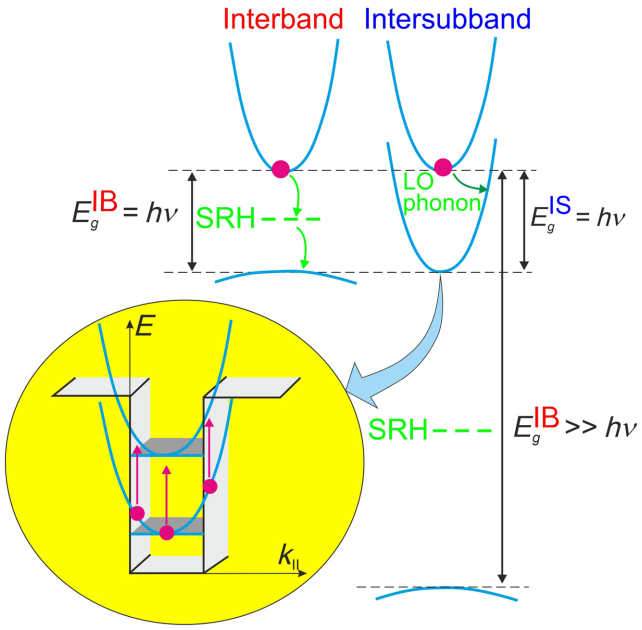

FIG. 6. Comparison of carrier recombination mechanisms in IB and IS photodetectors. For wide-band-gap-energy semiconductors, extrinsic Schockley-Read-Hall (SRH) defects have a decisive influence on the recombination mechanism. In the case of IS transitions, the main recombination mechanism is LO phonon emission (based on Ref. [22]).

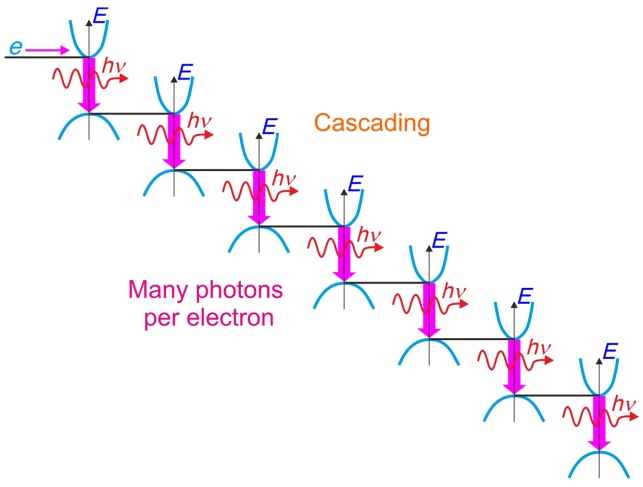

FIG. 7. Photon emission and cascade effect for an IB QCL (based on Ref. [23]).

2004 [9]. In the last 15 years, different IS QCP structures, over a wide spectral region from mid-infrared (MWIR) to terahertz (THz), have been demonstrated together with their applications in spectroscopy, pyrometry, and heterodyne astronomy [15–20]. Reviews of IS QCPs can be found in Refs. [21,22].

The operating principle of QWIP and IS QCP devices is highlighted in Fig. 5. QWIPs are photoconductive detectors where electrons in the lower level get excited to the upper state and conduct current through the continuum states above the conduction-band edge of the barrier. The active detector region consists of identical QWs separated by thicker barriers. Electrons are excited either by photoemission (red arrows) or by thermionic emission (black arrows) from the QWs. Symmetric QWIP devices operate in the presence of external bias. On the other hand, QCPs have built-in asymmetry in the band structure and operate at zero bias. As a consequence, the QCP is a photovoltaic detector. The QCP structures consist of several identical periods made of one active doped QW and some other coupled wells. The photoexcited electrons are transported from one active QW to the next one by phonon emission through a cascade of levels. Figure 5(b) shows the conduction band of one period. An incident photon induces an electron to transfer from the ground state, E_1, to the excited level, E_2, which is next transferred to the right QW through longitudinal optical phonon relaxations, and finally to the fundamental subband of the next period. The detector period is repeated N times to increase the responsivity.

Both QWIP and IS QCP devices are characterized by three essential features.

(i) They are unipolar majority-carrier devices where small effective band gaps are sandwiched between wider-gap semiconductors. The interband (IB) activation energy, E_g^{IB}, is much higher than the energy of detected photons, $h\nu = E_g^{\mathrm{IS}}$. The dark current is determined mainly by the small energy gap, E_g^{IS} (see Fig. 6). Due to large-band-gap semiconductors used in the QW structures, IS devices are self-passivated, which is a valuable advantage in comparison with narrow-gap semiconductor photodetectors.

(ii) A key factor affecting IS device performance is the light-coupling scheme. The IS selection rule requires that only the TM-polarization component of incident light scatters electrons between subbands (see Fig. 6). In the case of normal light incidence, the IS photodetectors are insensitive.

(iii) The main recombination mechanism in IS photodetectors is longitudinal (LO) phonon scattering with photocarrier lifetimes in the picosecond range. This means that QWIP and QCP devices are very fast, with transit-time cutoff frequencies in the 100-GHz range.

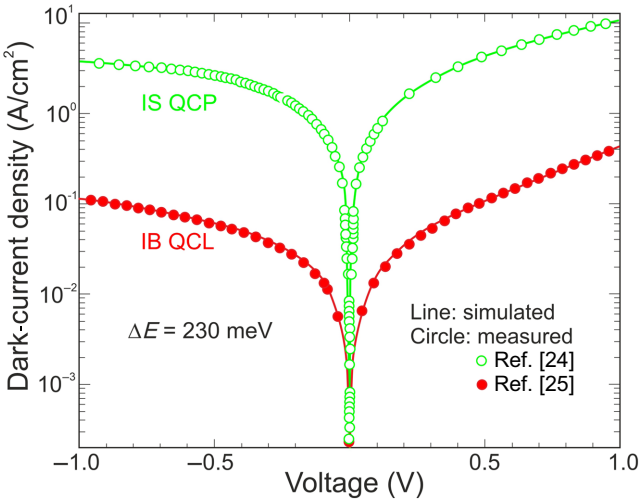

FIG. 8. Measured and fitted dark-current–voltage (I-V) characteristics of an 8-stage IB QCL and a 50-stage IS QCP with the same transition energy of 230 meV at 300 K (based on Refs. [24,25]).

C. Interband quantum cascade photodetectors

IB QCPs refer to the IB QCLs. The concept of the IB QCL was originally proposed in 1994 by Yang [23]. In this type of device, the manipulation of electron transport through an IB cascade scheme results in the generation of multiple photons by a single electron, as shown in Fig. 7. Unlike IS QCLs, in which photons are generated via an IS transition, IB QCLs use IB transitions.

The fundamental difference between the two types of cascade device results from fact that, for the IB QCLs, the injected carriers relax to the lower-energy level at a considerably slower rate than that for IS QCLs. IB QCL devices are intrinsic in their character, while IS QCL devices are extrinsic (doped). Similarly to common bulk semiconductors, the IB transitions in IB QCLs are characterized by radiative, Auger, and SRH g-r processes, where carrier lifetimes are in the order of nanoseconds. In contrast, IS relaxation for the QCLs is accompanied by LO phonon emission and falls in the picosecond range. Alternatively, IB QCPs are more sensitive to surface-leakage currents due to the presence of surface states in their band gap.

Figure 8 shows the measured and fitted dark-current–voltage characteristics of a large-area (400×400 μm^2) $N = 8$-stage IB QCL and an $N = 50$-stage IS QCP (110×110 μm^2) with the same 230-meV transition energy at 300 K [24,25]. The dark current is at least an order of magnitude lower for the IB device than that for the IS one.

The consequence of the much longer carrier lifetime for the IB QCP is also visible in the saturation current density, which in IB QCPs is almost 2 orders of magnitude lower than the values reached for IS QCPs (see Fig. 9) [26]. In addition, the threshold condition can be much easier to

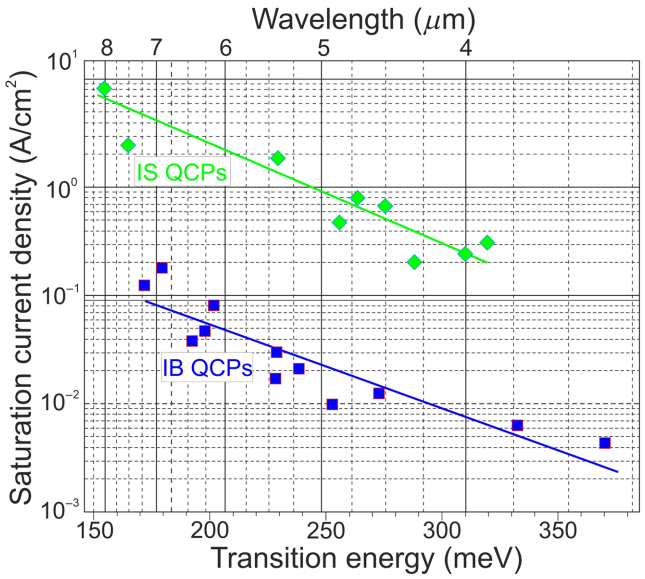

FIG. 9. Saturation current density for IS and IB QCPs at 300 K (based on Ref. [26]).

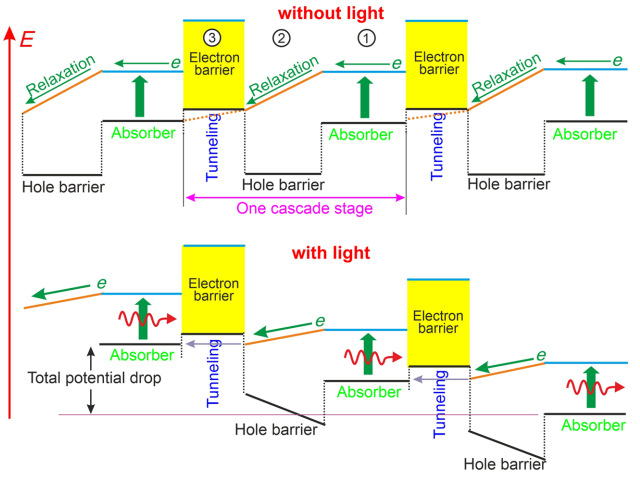

FIG. 10. Band diagrams of a multiple-stage IB photovoltaic device without and with illumination (based on Ref. [31]).

establish in IB QCLs. Moreover, in comparison with other types of MWIR lasers, such as Sb-based type-I QW diode lasers and $A^{IV}B^{VI}$ lead (Pb) salt lasers, the threshold current and input power of IB QCLs are considerably lower [27–30].

III. OPERATING PRINCIPLE OF INTERBAND QUANTUM CASCADE PHOTODETECTORS

The IB QCP operating principle is illustrated in Fig. 10. As shown, the device consists of multiple cascade stages. Each stage is divided into three zones based on three processes: (1) interband optical excitation, (2) intraband relaxation, and (3) interband tunneling. The stages are stacked in a way that is analogous to p-n junctions in multiple-junction solar cells. To provide proper carrier transport, the device is built of a compositionally graded semiconductor or digitally graded multiple QWs to form internal electric fields. In particular, one end of the conduction-band profile is required to be localized near the conduction band of the adjacent absorber. Similarly, the other end of the conduction-band profile should be near the valence band of the adjacent absorber. In contrast to a conventional p-n junction, only electrons can move through the intraband transport region because holes are confined to regions 1 and 3. Under illumination, as shown in the bottom part of Fig. 10, electrons move to the left, as a result of the asymmetry of the energy-band profiles in the transport region. Under steady-state conditions, the total potential drop (as a sum of sequential drops in each cascade) is created to balance the charge-carrier movement. In comparison with standard photodetector structures, the IB QCPs are more flexible, with multiple degrees of freedom for performance optimization.

A. Carrier collection

In comparison with a single-absorber device, an improvement in the carrier-collection efficiency, $f_c(x)$, is observed in the multiple-stage device. For example, Fig. 11 shows the distribution of the carrier-collection efficiency in the 3.3-μm-thick absorber versus distance x from the collection point ($x = 0$) for selected diffusion lengths. Assuming a diffusion transport model, the collection efficiency can be written as [32–34]

$$f_c(x) = \frac{\cosh[(d-x)/L]}{\cosh(d/L)}, \tag{1}$$

where d is the absorber thickness and L is the diffusion length. The results presented in Fig. 11 assume that light is incident from the collection point in the opposite direction to the flow of minority carriers. In the case when light is incident opposite to the collection point, the generation of electrons far from the collection point reduces the QE [35].

As expected, $f_c(x)$ is a strong function of diffusion length. In addition, it decreases dramatically versus x if the diffusion length is shorter than the absorber thickness. As shown in Fig. 11, an increase of the absorber thickness enhances the absorption; however, when the diffusion length is short, the QE is not improved.

The QE of a single-absorber device can be written as

$$\eta = \frac{q\int_0^d f_c(x) g_{\mathrm{ph}}(x)dx}{\Phi_o}, \tag{2}$$

where Φ_o is the incident-photon flux density per unit area, and $g_{\mathrm{ph}}(x)$ is the photon-generation rate per unit volume.

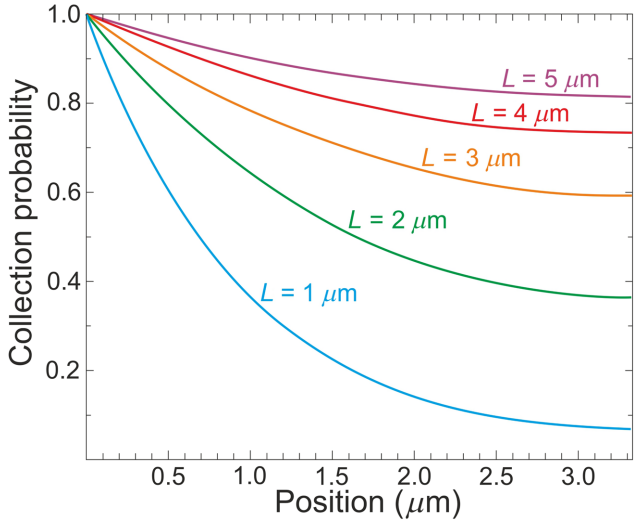

FIG. 11. Carrier-collection probability versus distance from the collection point for 3.3-μm-thick absorber for selected diffusion lengths (based on Ref. [32]).

As expected, $g_{\mathrm{ph}}(x)$ exponentially decreases with x:

$$g_{\mathrm{ph}}(x) = \Phi_o \exp(-\alpha x), \tag{3}$$

where α is the absorption coefficient.

Based on Eqs. (2) and (3), we can calculate the QE of a single-absorber device as

$$\eta = \frac{\alpha L}{1-(\alpha L)^2}\left[\tanh(d/L) + \frac{\alpha L \exp(-\alpha d)}{\cosh(d/L)} - \alpha L\right]. \tag{4}$$

Notably, Eq. (4) can be used to calculate the effective QE in the N-th stage of the cascade device. It is given by

$$\eta_N = \exp\left(-\alpha \sum_{m=1}^{N-1} d_m\right) \frac{\alpha L}{1-(\alpha L)^2} \times \left[\tanh(d_N/L) + \frac{\alpha L \exp(-\alpha d_N)}{\cosh(d_N/L)} - \alpha L\right], \tag{5}$$

where d_m is the absorber thickness in the m-th stage. An additional term in Eq. (5), in comparison with Eq. (4), represents light absorption in all upper stages above the m-th stage.

For the device with equal cascade stages, the incident-light intensity attenuates exponentially versus the absorption distance. As it propagates from the front to the back stages, the number of photogenerated carriers also decreases from the first front stage to the back stages. Consequently, the photocurrent, $I_{\mathrm{ph},m}$ ($m = 1, 2, 3, \ldots, N$), in each stage will not be equal. For example, Fig. 12 shows the decrease in I_{ph} for single-absorber and four-stage devices, assuming a low αL product ($\alpha L = 0.4$). The

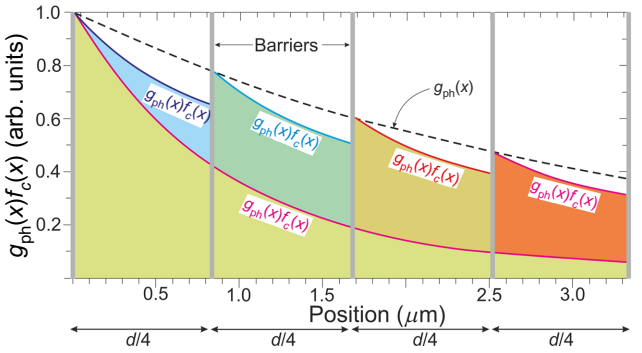

FIG. 12. Comparison of collection processes for $N = 1$-stage and $N = 4$-stage cascade devices for $\alpha L = 0.4$. Thickness, d, of the single-stage device is equal to the absorption depth. Thickness of individual absorber of $N = 4$-stage device is $d/4$ (based on Ref. [32]).

total absorber thickness for both structures is assumed to be the absorption depth, since no absorption occurs in the barrier regions. The absorption is significant only in the active region because the barriers are composed of semiconductor QWs with band gaps that are much wider than the absorber band gap.

As Fig. 12 shows, the areas of shaded regions for the two devices are different. The total effective QE of the $N = 4$-stage device is considerably higher than that of the $N = 1$-stage absorber device. This parameter is defined as the ratio of the total effective QE in any of the stages to the total absorption of incident photons, which is estimated to be $1-\exp(-\alpha d)$. As calculated by Huang, for the $N = 1$-stage absorber cell, it is only 46%, which, for the $N = 4$-stage device, reaches 89% [32].

The current responsivity of the photodetector is determined by the QE (η), and by the photoelectric gain, g. The QE describes how well the detector is coupled to the impinging radiation. It is defined here as the number of electron-hole pairs generated per incident photon in an intrinsic detector, the number of generated free unipolar charge carriers in an extrinsic detector, or the number of charge carriers with energy sufficient to cross the potential barrier in a photoemissive detector. The photoelectric gain is the number of carriers passing contacts per one generated pair in an intrinsic detector or the number of charge carriers in other types of detectors. This value shows how well the generated charge carriers are used to generate the current response of a photodetector.

The spectral current responsivity is equal to

$$R_i = q\frac{\lambda\eta}{hc}g, \tag{6}$$

where λ is the wavelength, h is Planck's constant, c is the speed of light, q is the electron charge, and g is the photoelectric current gain.

For a classical photoconductor, the basic expression to describe photoelectric current gain is

$$g = \frac{\tau}{t_t} = \frac{\tau}{l^2/\mu V}, \tag{7}$$

where t_t is the transit time of electrons between ohmic contacts, μ is the carrier mobility, and V is the voltage. This means that the photoconductive gain is given by the ratio of free carrier lifetime, τ, to transit time, t_t, between the electrodes. The photoconductive gain can be less than or greater than unity, depending upon whether the drift length, $L_d = v_d\tau$, is less than or greater than the interelectrode distance, l. The value of $L_d > l$ implies that a free charge carrier swept out at one electrode is immediately replaced by injection of an equivalent free charge carrier at the opposite electrode. Thus, a free charge carrier will continue to circulate until recombination takes place. In a multistage device with thin absorbers, the carrier transit time might be substantially shorter than the carrier lifetime, leading to electric gain, $g > 1$ [36,37].

As every cascade stage is connected in series, the current across each stage is required to be equal. This is reached by self-adjusting electric potentials across the stages, resulting from charge transfer at each stage. When there is no external voltage, the sum of these electric potentials is zero, i.e., $V_1 + V_2 + V_3 + \ldots + V_{N-1} + V_N = 0$. It is expected that the front stages with relatively large $I_{\rm ph}$ will be under a forward bias, such that a forward injection current will partially offset the photocurrent, while the back stage will be under a reverse bias, so that a thermal generation current will be added in those stages along the same direction as the photocurrent, resulting in an effective increase of the signal current to the external circuit. When the thermal generation current is higher than the photocurrent (which is possible at high temperatures), the stages under a reverse bias can have significant electric gains, as observed in the non-current-matched IB QCPs [37].

Based on the gain mechanism discussed above, the current can be expressed by

$$I_s = I_{{\rm ph},m} - I_o\left[\exp\left(\frac{qV_m}{kT}\right) - 1\right] \approx I_{{\rm ph},m} - I_o\frac{qV_m}{kT} = \sum_i^N I_{{\rm ph},i}/N, \tag{8}$$

where q is the electric charge; k is the Boltzmann constant; T is the temperature; V_m is the electric potential across the m-th stage; and I_o is the saturation dark current, which is identical in each stage for an equal-stage IB QCP. Since at high temperatures I_o is significantly higher than that photocurrent, the magnitude of the electric potential will be fairly small in each stage, and thus, the exponential terms in Eq. (8) can be expanded in a Taylor series with a first-order approximation in V_m. Based on Eq. (8), the electric potential across the m-th stage is given by

$$V_m = \frac{kT}{qI_oN}\left[NI_{{\rm ph},m} - \sum_i^N I_{{\rm ph},i}\right]. \tag{9}$$

This analytical expression indicates that the device current is the average of the photocurrents in each stage, as long as the dark current is considerably higher than the photocurrent. The electric gain enhances the signal current from the minimum photocurrent in the last stage to the average photocurrent across all stages.

B. Noise reduction in IB QDPs

The photodetector's multistage architecture offers an important advantage: a reduced noise level. As we see in Fig. 10, a single electron undergoes N interband excitations in an IB QCP to travel across the contacts. As a consequence, due to the averaging process, the noise current is reduced. Similarly to the IS transition in QWs, noise is reduced by a factor of $1/N$ (where N is the number of wells), if the emission and capture of electrons are uncorrelated in each QW [6,7].

A number of noise sources usually play important role in photoconductors. The fundamental types are Johnson-Nyquist (sometimes called thermal) noise, shot noise, g-r noise, and $1/f$ noise. In terms of LWIR photodetectors with a strong signal and low operating temperature, the dominant noise is related to the fluctuation of current induced by background radiation. Alternatively, when the signal is weak or the detector temperature is high, the detectivity is generally limited by shot or Johnson noise. Since these two noises are not coupled, the total mean-square-noise current is the sum of both noise currents:

$$i_n^2 = \frac{4kT}{R_o}\Delta f + 2qJ_dA\Delta f, \tag{10}$$

where R_o is zero-bias resistance, J_d is the dark-current density, Δf is the bandwidth, and A is the detector area. Then the detectivity is

$$D^* = \frac{R_i}{\sqrt{4kT/R_oA + 2qJ_d}}. \tag{11}$$

However, as mentioned above, the unipolar barriers allow IB QCPs to operate in unbiased mode, which indicates that shot noise can be neglected. Under these conditions, the detectivity is limited by Johnson noise and is called a

Johnson-noise-limited (JOLI) detector:

$$D^* = \frac{q\eta\lambda}{hc}\left(\frac{R_oA}{4kT}\right)^{1/2}. \quad (12)$$

As Eq. (12) shows, the most effective way to maximize detectivity is to increase the QE and the R_oA product, which equals $(\partial J_d/\partial V)^{-1}$ at zero bias.

The dark-current collection in the same direction as the photocurrent in the m-th stage in an IB QCP is equal:

$$J_{om} = q\int_0^d f_c(x)g_{\rm th}(x)dx = qg_{\rm th}L\tanh(d_m/L). \quad (13)$$

Here, $g_{\rm th}$ is the thermal generation rate per unit volume, which, unlike optical generation, is uniform across the device if each stage has an identical absorber band gap.

Assuming that thermal generation is the sum of Auger and SRH g-r mechanisms in the absorber region [38],

$$g_{\rm th} = \frac{n_i^2}{N_d\tau_A} + \frac{n_i^2}{(N_d+n_i)\tau_{\rm SRH}} = \frac{n_i^2}{N_d\tau}, \quad (14)$$

where

$$\frac{1}{\tau} = \frac{1}{\tau_A} + \frac{N_d}{N_d+n_i}\frac{1}{\tau_{\rm SRH}} \approx \frac{1}{\tau_A} + \frac{1}{\tau_{\rm SRH}}. \quad (15)$$

In Eqs. (14) and (15), N_d is the doping concentration, τ_A represents the carrier lifetime limited by the Auger g-r mechanism, and $\tau_{\rm SRH}$ is the SRH carrier lifetime. An approximation in Eq. (15) is valid if the doping concentration, N_d, is much higher than the intrinsic carrier concentration, n_i.

To maintain a constant current throughout all stages of the device, the other stages must have some compensating injection current. So, aside from the dark current, in the IB QCP, the injection current occurs in the opposite direction to that of the photocurrent. Its magnitude is equal to $J_{om}\exp(V_m/kT)$. In this situation, the total dark is

$$J_d(V) = qg_{\rm th}L\sum_{m=1}^{N}\tanh(d_m/L)\left[\exp\left(\frac{qV_m}{kT}\right)-1\right], \quad (16)$$

and the R_oA product is

$$R_oA = \frac{kT}{q^2g_{\rm th}L}\sum_{m=1}^{N}\frac{1}{\tanh(d_m/L)}. \quad (17)$$

For an IB QCP with identical stages, Eq. (17) can be simplified to

$$R_oA = \frac{kT}{q^2g_{\rm th}L}\frac{N}{\tanh(d_m/L)}. \quad (18)$$

Equations (17) and (18) indicate that the larger R_oA product is reached for more stages and thinner absorbers.

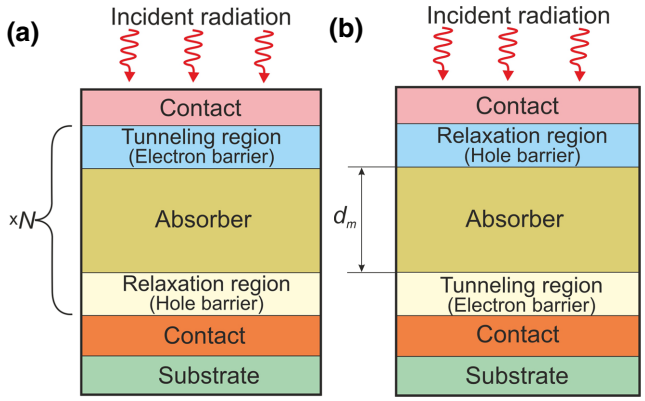

FIG. 13. Device structure for the IB QCPs: (a) regular illumination and (b) reverse-illumination configuration, where d_m is the absorber thickness in the m-th stage and N is the number of stages.

Taking into account Eqs. (10) and (11), we can conclude that the Johnson noise (detectivity) is lower (higher) in a multistage device compared with a single-absorber detector.

C. Optimal absorber thickness in IB QCPs

Generally, two types of architectures of IB QCPs can be distinguished based on the direction of incident radiation in relation to electron flow. In a regular designed device, photogenerated carriers and incident photons travel in the same direction, as shown in Fig. 13(a). In this case, the incident radiation goes through the electron barrier (EB) to the absorber region and then to the hole barrier (HB) in each stage, and most of the photocarriers are away from the collecting point (relaxation region). In a reversed-design architecture, photocarriers travel in the opposite direction to incident photons, through the HB to the absorber region and next to the EB [Fig. 13(b)]. In this situation, most of photocarriers are closer to the collection point, with shorter traveling distances in comparison with the regular-illumination configuration. As a consequence, due to the shorter transport distance, the reverse-illumination configuration results in a fast response time.

The QE of an identical-stage IB QCP device is determined by the stage with a minimum effective QE. Due to the most significant radiation attenuation, this is determined by the last stage and the external QE is equal to

$$\eta = \eta_d\exp[-\alpha d(N-1)], \quad (19)$$

where η_d is the QE of an individual stage. To include the influence of the surface reflectance, r, an additional factor $(1-r)$ should be added.

To maintain current continuity, there is additional injection current induced to offset the higher photocurrent in

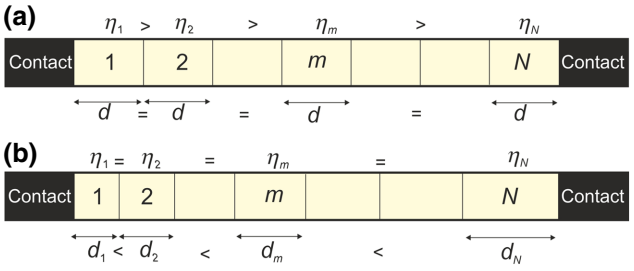

FIG. 14. Schematic diagram of a cascade photodetector with (a) equal and (b) matched absorbers.

other stages. This undermines some of the benefits provided by the multistage architecture.

To estimate the detectivity for the equal-stage device, we can use Eqs. (12) and (18) to derive

$$D^* = \frac{\lambda}{hc}\eta_{\text{ex}}\frac{\sqrt{N}}{\sqrt{4g_{\text{th}}L\tanh(d_m/L)}}, \tag{20}$$

where η_{ex} is the external QE given by expression (with photoelectric gain contribution) [34]

$$\eta_{\text{ex}} = \eta_d\frac{1-\exp(-\alpha N)}{1-\exp(-\alpha d)}\frac{1}{N}. \tag{21}$$

IB QCPs can also be classified in another way by either equal absorbers or matched absorbers. Both structures are schematically shown in Fig. 14.

In the second devices, the absorbers are chosen to collect an equal number of photons in each active layer. In this case, the individual absorber thicknesses increase from the first to the last stage to reach an equal photocurrent in each stage. In practice, however, perfect photocurrent matching is difficult to obtain, but, even with an inexact match in photocurrent, the QE can still be improved.

As mentioned previously, the photoelectric gain is related to the difference between the carrier lifetime and transit time. This type of gain is observed in the MWIR equal- and matched-absorber IB QCPs [37]. The second mechanism is typical for IB QCPs with equal absorbers and is connected to light attenuation in subsequent stages.

The detectivity enhancement in IB QCPs has been considered by Hinkey and Yang [34]. Substituting Eq. (17) into Eq. (12), the Jonson-noise-limited detectivity can be expressed by

$$D^* = \frac{\lambda}{hc}(4g_{\text{th}}L)^{-1/2}\eta\sum_{m=1}^{N}1/\tanh(d_m/L). \tag{22}$$

Using Eq. (22), the absorber thickness is determined to obtain the optimal photocurrent-matched absorber and maximum detectivity. Figure 15 shows the calculated detectivity enhancement versus αL product for devices

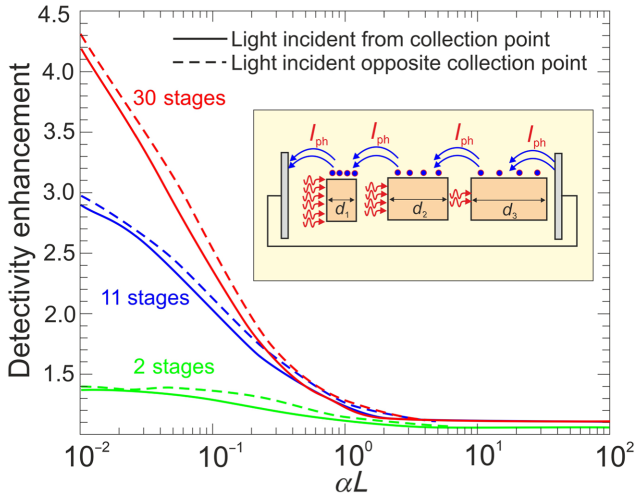

FIG. 15. Johnson-noise-limited detectivity enhancement for current-matched IB QCPs with 2, 11, and 30 stages (based on Ref. [34]).

with 2, 11, and 30 stages. The detectivity enhancement is defined as $D^*(N)$ of the optimized multistage IB QCPs normalized to the value $D^*(1)$ of the optimized single-absorber detector. As shown, the detectivity increases versus number of stages due to noise suppression, although the signal current is slightly reduced. In addition, the pronounced detectivity enhancement is observed for $\alpha L < 1$; however, for higher αL, multistage IB QCPs do not improve the performance, since the upper improvement is about 1.1 times higher than that of single-absorber photodetectors.

If the photodetector operates under a reverse bias, the shot noise due to the dark current should be included in the detectivity. As shown by Yang *et al.*, the shot noise is reduced in IB QCPs with more stages, since the S/N ratio is proportional to $\sqrt{N}$ [38]. Then

$$D^* = \frac{R_i}{\sqrt{(4kT/RA)+(2qJ_d/N)}}, \tag{23}$$

where R_i, J_d, RA, and N are the device responsivity, dark-current density, dynamic resistance area product, and the number of stages, respectively.

Bipolar devices based on T2SL materials, such as InAs/GaSb and InAs/(In, As)Sb, are good candidates for IB QCPs operating near room temperature [34–49]. For this reason, further considerations, together with simulation results, are given for those devices.

Hackiewicz *et al.* provided theoretical calculations of IB QCPs optimized for 3.3 μm and operating at 300 K. It is obvious that the penetration depth of the radiation should be comparable to the total thickness of the absorbers. The thickness of each m stage, d_m, should be carefully designed [49].

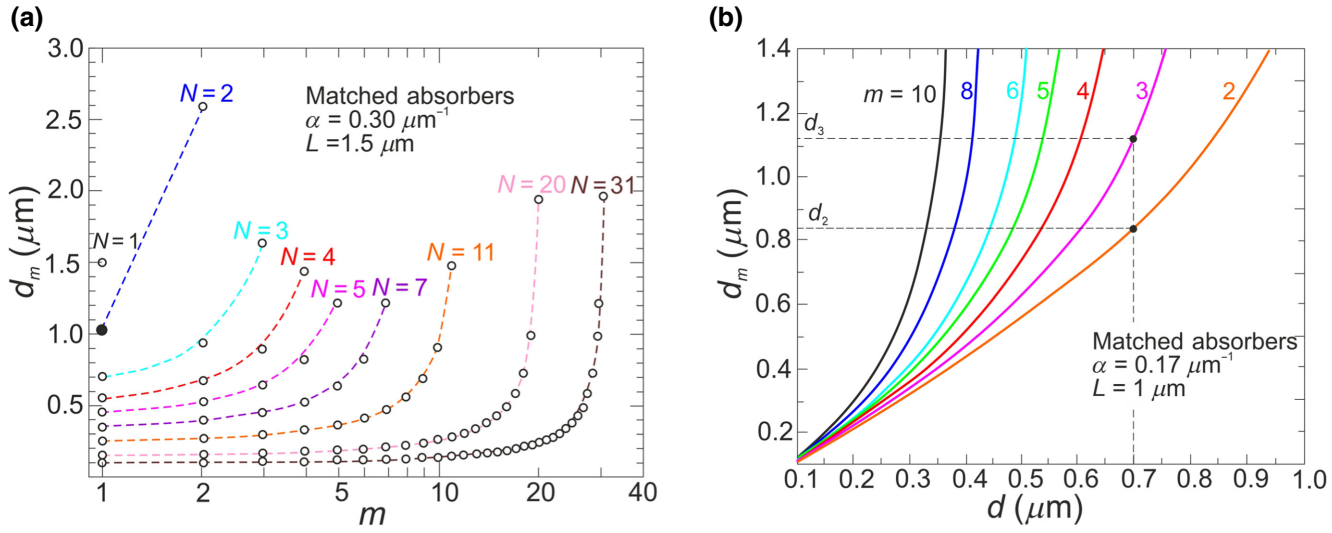

FIG. 16. Absorber thickness, d_m, in subsequent stages (m) in matched-absorber IB QCPs versus (a) number of subsequent stages m (based on Ref. [48]), (b) versus first-absorber thickness, d (based on Ref. [49]).

For example, Fig. 16(a) shows the absorber thickness in subsequent stages (m) for the matched-absorber photodetector versus number of stages, m, assuming an absorption coefficient of $\alpha = 0.3\ \mu\text{m}^{-1}$ and a diffusion length of $L = 1.5\ \mu$m. We can see that, when the thin first absorber is selected, the remaining thickness is essentially constant, and the requirement for QE is met for a very large number of stages. For the device with $N = 31$ stages and thickness $d_1 = 0.1\ \mu$m, the last absorber is 1.97 μm thick; however, the largest first absorber to fulfil the QE condition to make another stage is 1.03 μm thick (black filled dots) [49].

The LWIR T2SL photodetectors are characterized by a lower αL product than those of the MWIR ones considered above. On account of this, in simulations of LWIR devices with a cutoff wavelength of $\lambda_{\text{cutoff}} = 10\ \mu$m, it is assumed that $\alpha = 0.17\ \mu\text{m}^{-1}$ and $L = 1\ \mu$m [49]. Figure 16(b) shows the influence of the first active layer in the equal absorbers on the thickness of a subsequent one. As shown, the first-absorber thickness increases and the number of stages decreases. For the first 0.7-μm-thick absorber, only the next two stages are possible, and the maximum number of cascades is $N = 3$.

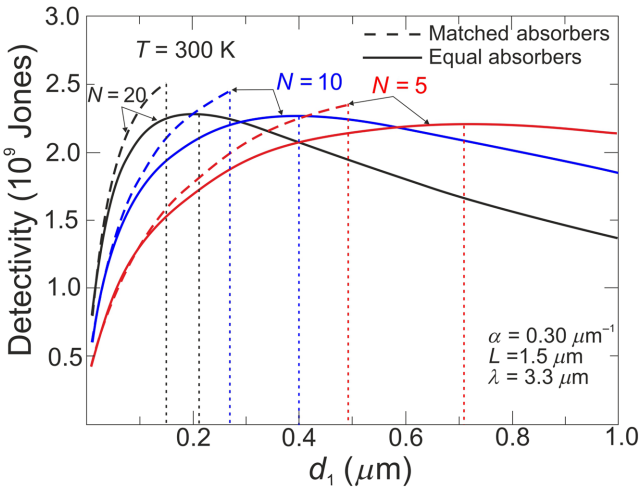

FIG. 17. Detectivity versus first-stage absorber thickness for $N = 5$, 10, and 20 stages. Dashed lines refer to detectors with matched absorbers and solid lines to detectors with equal absorbers (based on Ref. [48]).

Figure 17 presents the theoretical dependence of detectivity on the first-stage absorber thickness for matched-absorber and equal-absorber IB QCPs with a selected number of stages. Additionally, in simulations of the equal-absorber devices, the electric current gain is included [48].

Figure 17 shows that the optimal thickness of the first absorber is higher for equal absorbers than that for matched absorbers, but the maximum detectivity is slightly lower. It is expected that, since matched-absorber devices have to meet the QE condition, their total thicknesses should be higher in comparison with equal-absorption devices. For example, for the $N = 10$-stage equal absorbers, the total thickness is 4 μm, while for matched-absorber devices this increases to 5.7 μm. For both analyzed structures, the detectivity increases versus absorber thickness despite the noise increase in thicker absorbers being related to an increase in QE. It should be mentioned, however, that matched absorbers are more challenging to fabricate and a slightly higher maximum detectivity does not compensate for technological difficulties. From Fig. 17, we can estimate d_{opt} of the first absorbers (vertical lines) for which detectivity is maximized. This figure also indicates that, as N increases, the maximum detectivity more strongly depends on the deviation of d_1 from $d_{1\text{opt}}$.

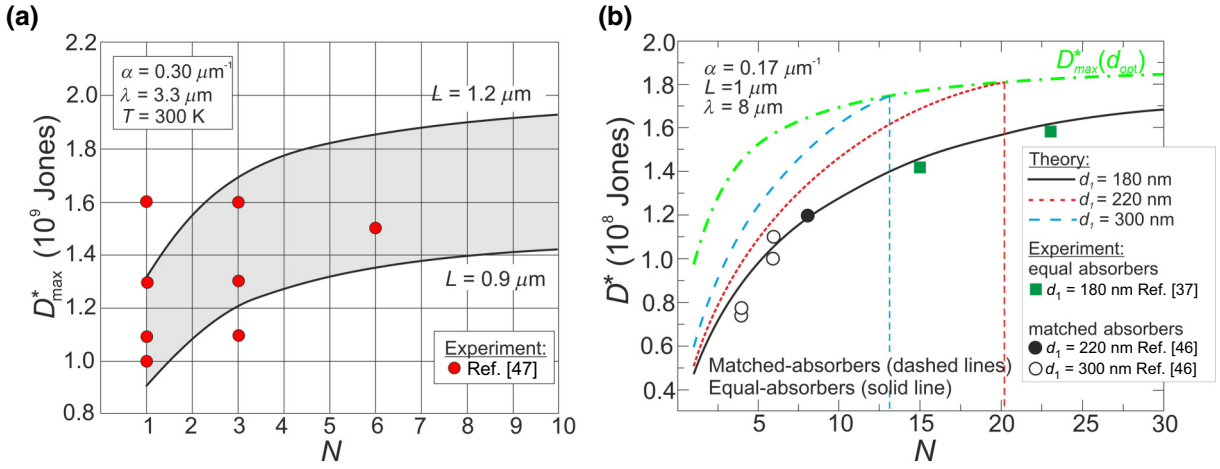

FIG. 18. Room-temperature detectivity versus number of stages for (a) matched-absorber photodetectors at $\lambda = 3.3$ μm (based on Ref. [48]) and (b) equal-absorber and matched-absorber photodetectors at $\lambda = 8$ μm (based on Ref. [49]). Experimental data are given in the inset. Green dashed-dotted line presents D^*_{max} for photodetectors with optimal absorber, d_{opt}.

Figure 18 compares theoretical estimates of maximum detectivity with experimental data for two types of IB QCPs with MWIR and LWIR absorbers based on the InAs/GaSb T2SLs. Most of the experimental results are in the filled gray area and correspond to theoretical D^*_{max}, assuming a diffusion length of $L = 0.9$–1.3 μm. A certain dispersion of experimental points beyond the gray area may result from material nonuniformity during device fabrication. It is expected that, as the number of relatively thin stages increases, the experimental detectivity decreases due to a shortening of the diffusion length [48].

Generally, the theoretical estimates for LWIR devices presented in Fig. 18(b) coincide well with experimental data. The dashed lines are related to the matched-absorber photodetectors, with the first absorber being similar to experimental values: 220 and 300 nm [46]. The solid line is calculated for an equal-absorber photodetector with $d_1 = 180$ nm [37]. The detectivities for both types of devices are comparable. For the LWIR IB QCPs, the total thickness of matched-absorber photodetectors is typically 2 times higher than that for equal absorbers with zero electric gain [49].

IV. TYPE-II SUPERLATTICE MATERIALS USED IN IB QCP FABRICATION

It is shown that the ratio of the absorption coefficient (α) to the thermal generation rates (g_{th}), α/g_{th}, is the main

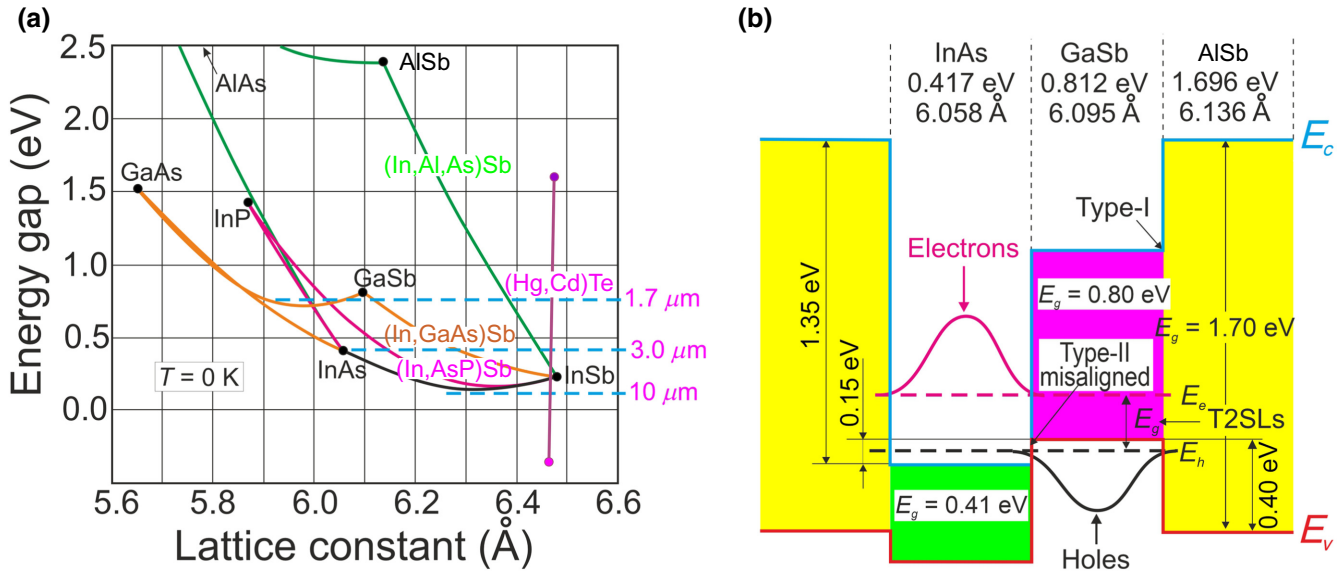

FIG. 19. Band-gap energy and wavelength diagram of $A^{III}B^{V}$ semiconductor material systems at 0 K (a). Schematic illustration of low-temperature energy-band alignment in the nearly 6.1-Å lattice-matched InAs/GaSb/AlSb material system (b).

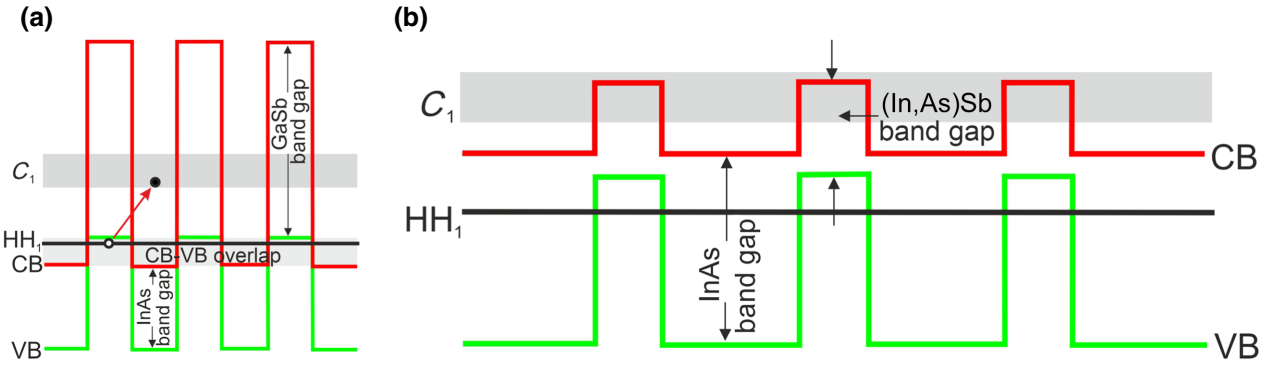

FIG. 20. Band-gap diagram for T2SLs: (a) InAs/GaSb and (b) InAs/(In, As)Sb (based on Ref. [55]).

figure of merit of any material for IR photodetectors, since the detectivity [50],

$$D^* \propto \frac{\lambda}{hc}\left(\frac{\alpha}{g_{\text{th}}}\right)^{1/2}, \tag{24}$$

is proportional to $(\alpha/g_{\text{th}})^{1/2}$, where λ is the wavelength, h is Planck's constant, and c is the speed of light. The thermal generation rate is inversely proportional to the net carrier lifetime (τ) [see Eq. (14)] and, in turn, D^* is proportional to $(\alpha\tau)^{1/2}$; these are two fundamental parameters of semiconducting materials used in the fabrication of the detector's active region.

The operation of bipolar interband cascade photodetectors is made possible by the unique properties of the 6.1-Å $A^{\text{III}}B^{\text{V}}$ material systems, InAs, GaSb, and AlSb, and their related alloys and SLs. One of the unusual properties of these materials is the type-II broken-gap alignment between InAs and GaSb. In this section, first, the fundamental physical properties are described briefly. This topic is covered in detail in monographs and review papers [38,51–54]. The second part of the section is devoted to a brief description of the growth and fabrication of multistage devices.

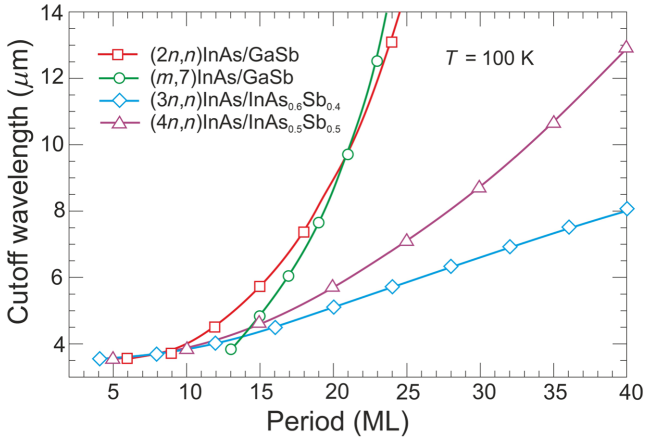

FIG. 21. Theoretically estimated λ_{cutoff} for (2n,n)-InAs/GaSb, (m, 7)-InAs/GaSb, (3n,n)-InAs/InAs$_{0.6}$Sb$_{0.4}$, and (4n, n)-InAs/InAs$_{0.5}$Sb$_{0.5}$ SLs at 100 K (all on GaSb substrate) versus SL period in MLs (based on Ref. [56]).

A. Fundamental properties

As shown in Fig. 19, the binary $A^{\text{III}}B^{\text{V}}$ semiconductors InAs, GaSb, and AlSb belong to the 6.1-Å semiconductor family of closely lattice-matched compounds with lattice constants of 6.0584, 6.0959, and 6.1355 Å, respectively. Thus, these binary materials can be incorporated into the same heterostructure with low densities of defects and dislocations.

The 6.1-Å semiconductor family (InAs, AlSb, GaSb) crystallizes in the zinc blende (ZB) structure. The band gaps of related alloys are between 0.41 eV (for InAs) and 1.70 eV (for AlSb) at room temperature. InAs, GaSb, and AlSb SLs exhibit type-II misaligned-band offsets between InAs and GaSb. As shown in Fig. 19(b), the CB edge of InAs is about 150 meV lower than the VB edge of GaSb, creating a spatial separation of electrons and holes in the InAs/GaSb heterostructure.

The band-gap alignments shown in Fig. 19 indicate additional benefits: the InAs/AlSb interface forms a type-II staggered alignment, where the CB edge of InAs is slightly above the VB edge of AlSb. An extremely large conduction-band offset, nearly 1.45 eV at room temperature, enables the realization of very deep QWs and large tunneling barriers. For this reason, InAs/AlSb heterostructures are frequently used in resonant tunneling diodes and SWIR QCLs.

Figure 20 shows that the T2SL band alignment is different from the more widely studied type-I superlattice (Al,Ga)As/GaAs system. The flexibility in energy-band-gap tuning of the SLs from either a semimetal (for wide InAs and GaSb layers) or a narrow-band-gap (for narrow layers) semiconductor is of great interest for the design of photodetectors operating over a wide spectral range. The band gap is determined by the energy difference between the electron miniband, C_1, and the first heavy-hole state,

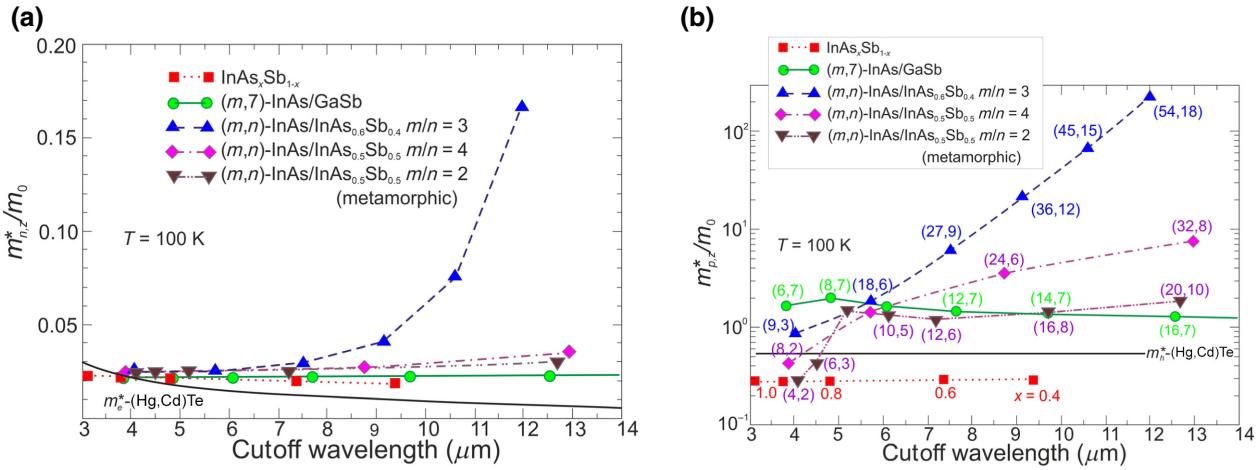

FIG. 22. Electron (a) and hole (b) effective masses along the growth direction versus λ_{cutoff} for selected material systems: free-standing bulk (In, As)Sb with varying Sb composition x, $(m, 7)$-InAs/GaSb T2SL, pseudomorphic (m, n)-InAs/$InAs_{0.6}Sb_{0.4}$ T2SL on GaSb substrate, pseudomorphic (m, n)-InAs/$InAs_{0.5}Sb_{0.5}$ T2SL on GaSb substrate, and (m, n)-InAs/$InAs_{0.5}Sb_{0.5}$ T2SL on a metamorphic substrate with a lattice constant 0.4% larger than that for GaSb (based on Ref. [56]).

HH_1, at the Brillouin-zone center. The electron's effective mass (m_e^*) is considerably lower than the hole's effective mass (m_h^*), and thus, the C_1 band is more sensitive to layer thickness than HH_1. The thickness of the GaSb layers has a negligible influence on the T2SL band gap due to the large GaSb heavy-hole mass ($\sim$0.41 m_o); however, the thickness of GaSb has a significant impact on the conduction-band dispersion due to penetration of the InAs electron wave functions into the GaSb barriers. In addition, the SL band gap depends on the strain effects because binary compounds are not exactly lattice matched.

InAs/GaSb and InAs/(In, As)Sb SLs have the following fundamental properties:

(i) both T2SLs are based on nearly-lattice-matched $A^{III}B^{V}$ semiconductors and provide a large range of tunability in λ_{cutoff};

(ii) the electron and hole wave functions are located in separate layers;

(iii) the band offsets in conduction (ΔE_c) and valence (ΔE_v) bands in the InAs/GaSb SL ($\Delta E_c \sim 930$ meV, $\Delta E_v \sim 510$ meV) are much larger than those of the InAs/(In, As)Sb SL ($\Delta E_c \sim 142$ meV, $\Delta E_v \sim 226$ meV);

(iv) the InAs/GaSb SL's much larger broken gap makes it easier to reach low SL band gaps;

(v) as the period increases, λ_{cutoff} of the InAs/GaSb SL increases much faster than that of the InAs/(In, As)Sb SL; the shorter period of the InAs/GaSb SL gives the same λ_{cutoff} as that of the InAs/(In, As)Sb SL.

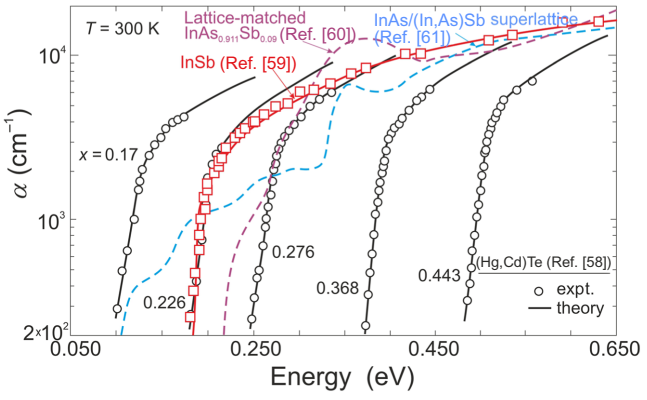

FIG. 23. Comparison of intrinsic absorption coefficients for InSb and $Hg_{1-x}Cd_xTe$ with lattice-matched $InAs_{0.911}Sb_{0.09}$ and InAs/(In, As)Sb SLs at room temperature (based on Refs. [58–61]).

Figure 21 shows the theoretically predicted λ_{cutoff} versus SL period for strain-balanced (with respect to the GaSb substrate) InAs/GaSb and InAs/(In, As)Sb T2SLs. To reach strain balance between InAs/GaSb SLs layers, (In, As)Sb interfacial monolayers (MLs) are inserted between the InAs and GaSb layers. As shown in Fig. 21, the $(m,n)A/B$ denotation indicates SLs with "m" MLs of material "A" and "n" MLs of material "B" in each period of $(m + n)$ MLs.

T2SLs are characterized by asymmetrical transport properties. The effective mass along the growth direction is considerably larger than that for bulk semiconductors, particularly in LWIR T2SLs, leading to low mobility, short diffusion length, and low collection efficiency n-type devices. Figure 22 shows theoretically predicted values of m_e^* and m_h^* for bulk (In, As)Sb and both InAs/GaSb and InAs/(In, As)Sb T2SLs versus typical MWIR and LWIR ranges. In properly designed T2SLs, m_e^* is comparable to

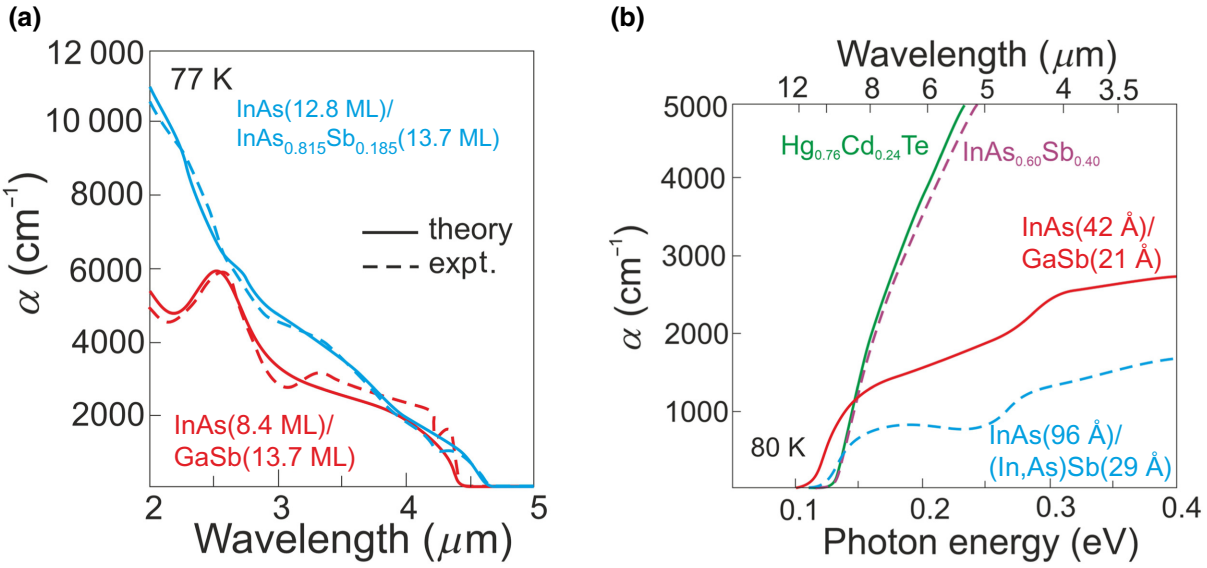

FIG. 24. Experimental and theoretical absorption spectra for MWIR InAs/GaSb and InAs/(In, As)Sb T2SLs at 77 K (a) (based on Ref. [62]) and LWIR (Hg, Cd)Te and selected $A^{III}B^{V}$ material systems at 80 K (based on Ref. [63]). (b) Calculated interband absorption coefficients for bulk $InAs_{0.60}Sb_{0.4}$; $Hg_{0.76}Cd_{0.24}Te$; and InAs(42 Å)/GaSb(21 Å), InAs(96 Å)/$InAs_{0.61}Sb_{0.39}$ (29 Å), and $InAs_{0.66}Sb_{0.34}$(11 Å)/$InAs_{0.36}Sb_{0.64}$(12 Å) T2SLs.

that of the bulk material, while, in the LWIR region, m_h^* along the growth direction is larger than that in the bulk material. For example, in comparison with (Hg, Cd)Te, exhibiting a band gap of $E_g \approx 0.1$ eV and $m_e^*=0.009m_0$, the T2SL's m_e^* is larger.

Interest in T2SL InAs/(In, As)Sb is related to the carrier-lifetime limitations imposed by the GaSb layer in InAs/GaSb SLs. For materials with the same λ_{cutoff}, a significantly longer minority-carrier lifetime is reached for the InAs/(In, As)Sb SLs in comparison with the InAs/GaSb SLs. Typical carrier lifetimes at 77 K for MWIR materials are about 1 μs and about 100 ns for Ga-free SLs and InAs/GaSb SLs, respectively. An increase in minority-carrier lifetime suggests a lower dark current for InAs/(In, As)Sb SL photodetectors in comparison with InAs/GaSb SL ones.

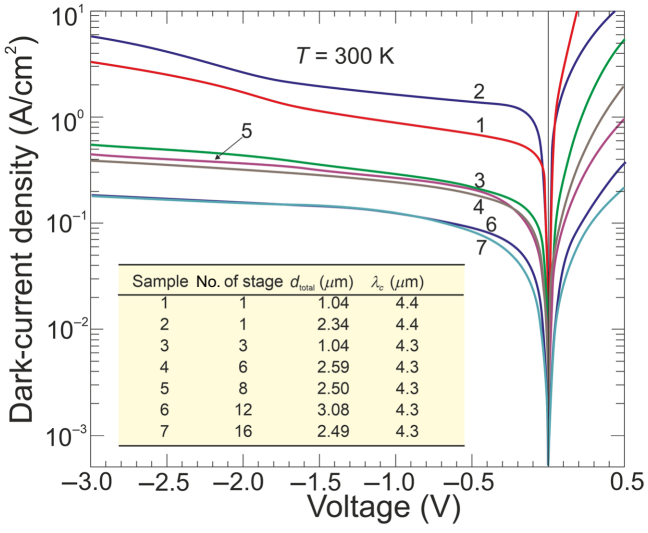

FIG. 25. Dark-current density versus voltage for several MWIR IB QCPs operating at room temperature (based on Ref. [66]).

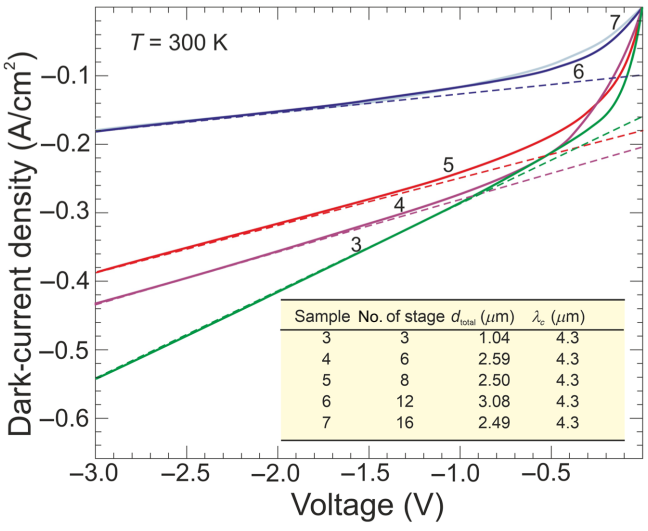

FIG. 26. Linear fitting (dashed) and experimental measurements (solid) of dark-current density at reverse bias for five multistage devices at 300 K. Number of samples is the same as that in Fig. 25 (based on Ref. [66]).

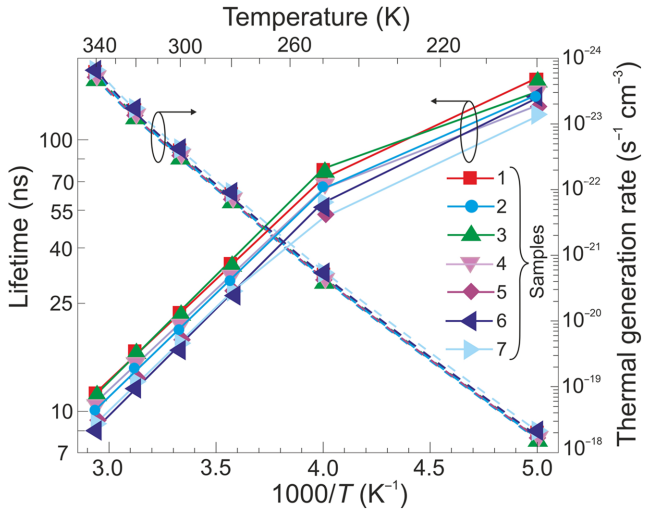

FIG. 27. Thermal generation rate and minority-carrier lifetime for multistage devices under HOT conditions. Number of samples is the same as that in Fig. 25 (based on Ref. [66]).

T2SL InAs/GaSb band alignment results in an overlap energy (estimated to be 140–170 meV) between the CB minimum and the VB maximum of the two materials. For T2SL InAs/(In, As)Sb, the estimated band offset is about 620 meV. The primary difference in the CB and VB profiles in T2SL InAs/GaSb and InAs/(In, As)Sb is illustrated in Fig. 20. The band offsets in the CB (ΔE_c) and VB (ΔE_v) in the (In, As)Sb SL ($\Delta E_c \sim 142$ meV, $\Delta E_v \sim 226$ meV) are much smaller than those for the InAs/GaSb SL ($\Delta E_c \sim 930$ meV, $\Delta E_v \sim 510$ meV) [38, 57]. This situation suggests a higher contribution of the tunneling mechanism in the net dark current for the T2SL InAs/(In, As)Sb photodiodes at a HOT.

The detectivity of the IR photodetector is proportional to $(\alpha\tau)^{1/2}$, so the spectral dependence of the absorption coefficient has a strong influence on both the QE and D^*. The InAs/(In, As)Sb T2SLs, with an average lattice constant matching that of GaSb have significantly lower absorption than that of bulk (Hg, Cd)Te and InAs/GaSb SLs (see Figs. 23 and 24). The shape of the LWIR α edge depends on the overlapping of the electron-hole wave functions, which, in the case of the InAs/(In, As)Sb T2SL, occurs primarily in the well for holes with a relatively small thickness throughout the SL period. As shown in Fig. 24, the InAs/GaSb SLs exhibit more favorable oscillator strengths and absorption coefficients than those of InAs/(In, As)Sb SLs, especially in the VLWIR spectral range. However, due to weaker confinement of the CB, more delocalized electron wave functions help somewhat in enhancing the absorption properties of the InAs/(In, As)Sb T2SLs. Generally, a shorter SL period provides a larger absorption coefficient due to better wavefunction overlap and greater oscillator strength.

The experimental and theoretical absorption coefficients for InAs/GaSb and InAs/(In, As)Sb T2SLs presented in Fig. 24(a) coincide well for the / InAs(12.8 ML)/(In, As)Sb(12.8 ML) SL and for the InAs(8.4 ML)/GaSb (13.7 ML) SL; however (see Fig. 23), the (Hg, Cd)Te absorption coefficient is stronger than those of both T2SLs [62,63]. In addition, theoretical estimates of the absorption spectra for LWIR T2SLs and bulk materials [(Hg, Cd)Te and (In, As)Sb] support the above observations [see Fig. 24(b)] [63]. In addition, these estimates show that the absorption coefficient is only comparable with bulk materials for the small-period metamorphic $InAs_{1-x}Sb_x/InAs_{1-y}Sb_y$ SLs.

To date, the InAs/(In, As)Sb T2SLs are less studied than their InAs/GaSb counterpart. Due to only two common elements (In and As) in the SL layers and a relatively simple interface structure upon changing the Sb element, growth of the InAs/(In, As)Sb T2SLs is characterized by better controllability and simpler manufacturability.

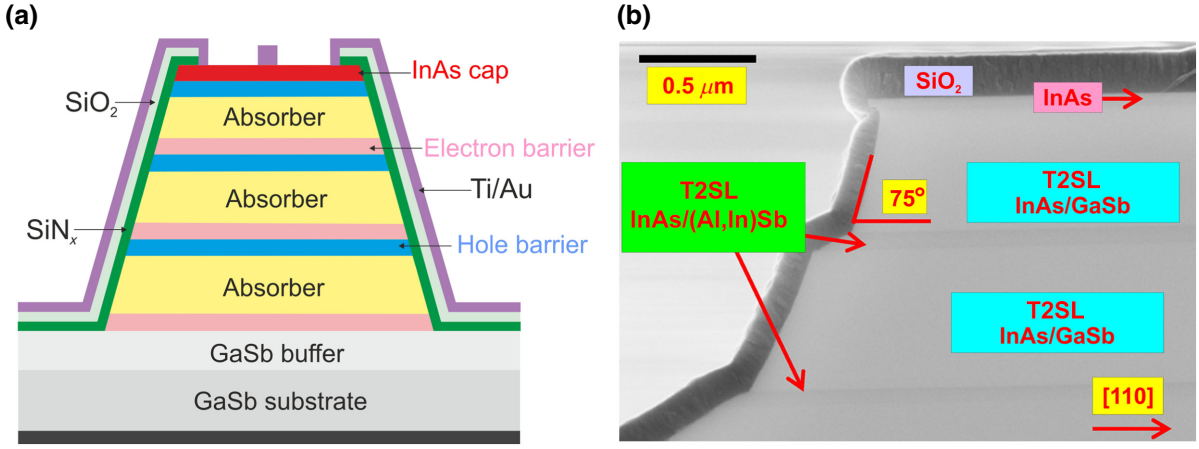

FIG. 28. IB QCP cross section: (a) schematic of $N = 3$-stage fabricated device, (b) scanning electron microscope image of a wet-etched device structure (based on Ref. [73]).

TABLE I. T2SL barrier detectors.

Flat-band energy diagrams	Example of detector structure	Description
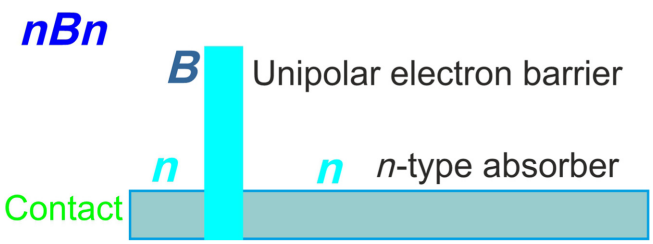	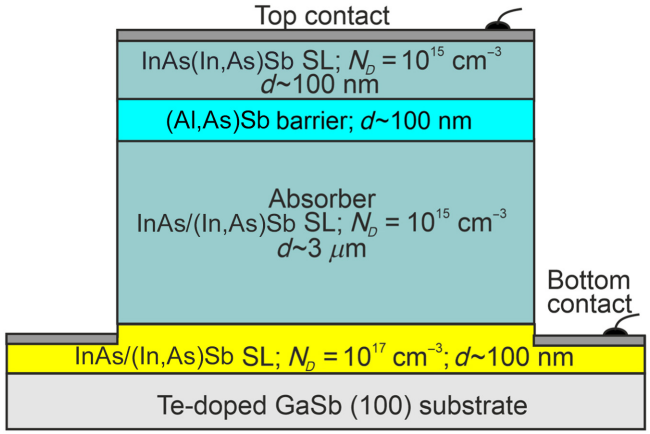	Top-contact, absorber, and bottom-contact layers are composed of T2SL InAs/(In, As)Sb. As a unipolar barrier located between the top contact and absorber, 100-nm-thick (Al, As)Sb Be-doped to 10^{15} cm^{-3} is used. Top contact and absorber layers are not intentionally doped (n.i.d.) while the bottom contact is Te-doped to a level of 10^{17} cm^{-3} [74].
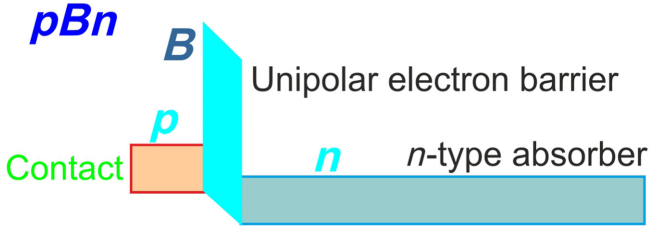	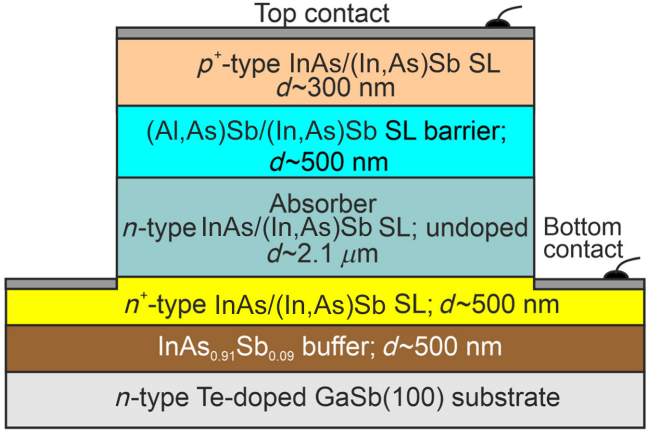	Structure is constructed from a 700-nm-thick n^+-doped $GaSb/InAs_{0.91}Sb_{0.09}$ buffer layer, upon which a 500-nm-thick n^+-doped bottom-contact layer, a 2.1-μm n.i.d. active layer, a 500-nm electron barrier, and a 300-nm-thick p-type top contact are deposited. Top and bottom contacts and the active layer are composed of T2SL InAs/(In, As)Sb. Si and Be are used for n-type and p-type dopants, respectively [75].

TABLE I. T2SL barrier detectors.

Flat-band energy diagrams	Example of detector structure	Description
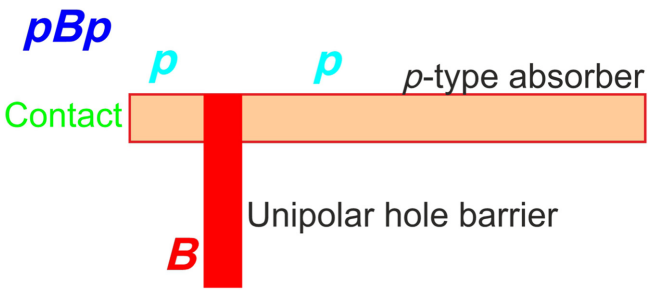	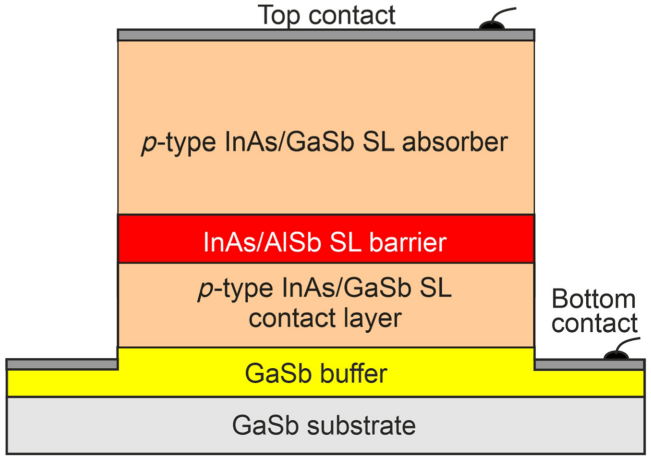	Contact layers and absorber are composed of T2SL InAs/GaSb. Barrier layer is based on T2SL InAs/AlSb. Proper lattice matching to the GaSb substrate is ensured by InSb-like interfaces [76].
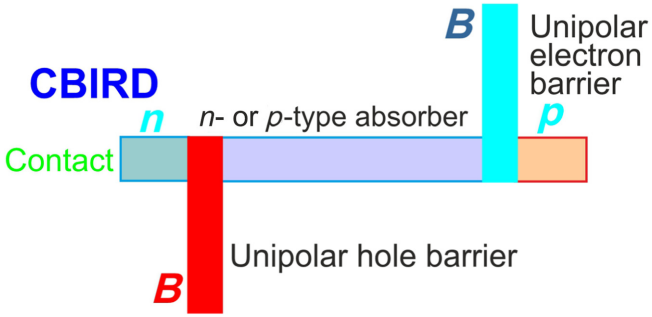	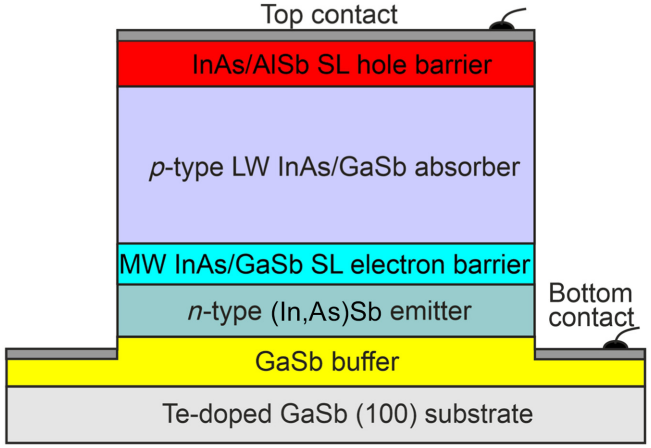	Detector is composed of a lightly p-type T2SL InAs/GaSb active layer being sandwiched between n-type T2SL InAs/AlSb HB and a wider T2SL InAs/GaSb EB. Barriers are designed to exhibit zero conduction band offset (CBO) and valence band offset (VBO) in relation to the active layer. Heavily doped n-type (In, As)Sb layer adjacent to the EB plays the role of the bottom contact. SRH g-r and trap-assisted tunneling (TAT) are reduced by the N-p heterojunction between the HB and active layer [77].

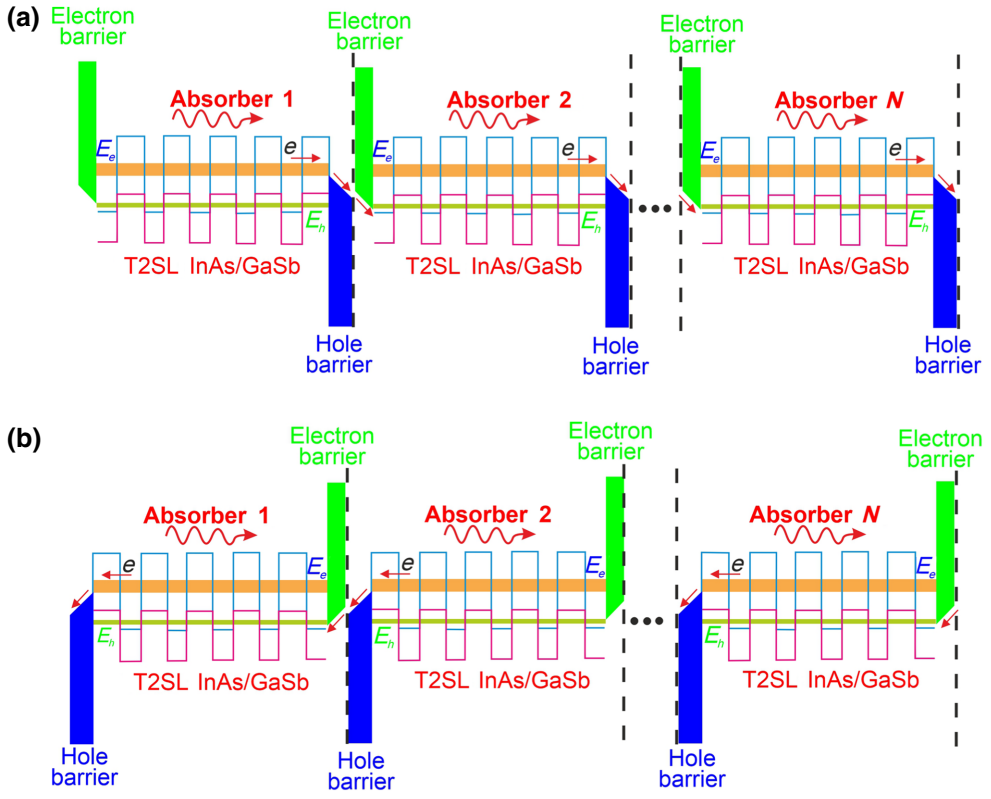

FIG. 29. Schematic band diagram of N-stage IB QCPs with (a) regular and (b) reverse configurations (based on Ref. [35]).

B. Carrier lifetime

As mentioned in Sec. IV A, the main drawback of InAs/GaSb T2SLs is the short carrier lifetime, typically in the range between 10 and 100 ns, which is mainly limited by the SRH g-r [38]. The origin of the SRH g-r is related to the presence of Ga, as the Ga-free InAs/(In, As)Sb SLs exhibit much longer carrier lifetimes, above 400 ns [64,65].

Usually, to estimate carrier lifetime, optical methods based on time- or frequency-domain photoluminescence measurements are used. The research group at the University of Oklahoma (OU) elaborated a simple and effective electric method to extract the carrier lifetimes of InAs/GaSb SLs used in the fabrication of IB QCPs. Equation (16) shows that the dark current in the m-th stage of an IB QCP can be written as

$$J_{d,m}(V) = qg_{\text{th}}L\tanh(d_m/L)\left[\exp\left(\frac{qV_m}{kT}\right)-1\right], \quad (25)$$

where V_m is the voltage across the m-th stage. This equation is valid if the parasitic series resistance, R_s, and shunt resistance, R_{shunt}, are negligible. In an equal-absorber device, the voltage drop across each stage is V/N.

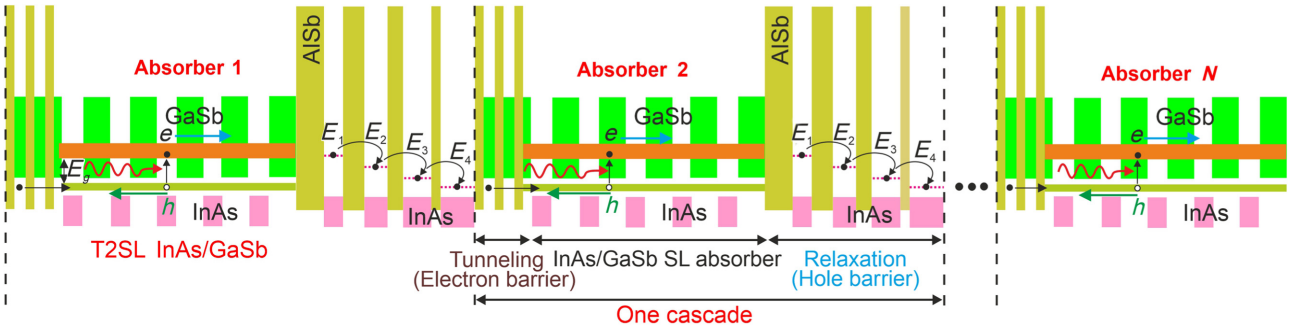

FIG. 30. Schematic illustration of a regular IB QCP configuration with T2SL InAs/GaSb absorber, GaSb/AlSb tunneling, and InAs/AlSb relaxation layers.

TABLE II. Summary of design and material parameters for MWIR wafers (based on Ref. [47]).

Wafer	Config. (see Fig. 29)	N	Absorber thickness (nm)	Total absorber thickness (nm)	p-Type doping in absorber (cm^{-3})	p-Type doping in buffer (cm^{-3})	p-Type doping in absorber (cm^{-3})	Surface-defect density (cm^{-3})
R146	Reg.	8	253.5, 279.5, 312, 344.5, 383.5, 435.5, 500.5, 591.5	3100.5	3.8×10^{16}	3.2×10^{17}	1.6×10^{17}	5×10^{4}
Y004D	Rev.	3	312, 344.5, 383.5	1040	5.1×10^{16}	2.8×10^{17}	2.6×10^{16}	3×10^{4}
Y005D	Rev.	3	312, 344.5, 383.5	1040	5.1×10^{16}	5.1×10^{17}	2.6×10^{16}	2×10^{4}
Y007D	Rev.	1	1040	1040	5.1×10^{16}	2.8×10^{17}	2.6×10^{16}	3×10^{4}
Y008D	Rev.	6	312, 344.5, 383.5, 435.5, 507, 604.5	2587	3.8×10^{16}	2.9×10^{17}	2.6×10^{16}	2×10^{4}
Y009D	Rev.	8	312×8	2496	3.8×10^{16}	2.9×10^{17}	2.6×10^{16}	5×10^{4}
Y010D	Rev.	3	507, 617.5, 793	1917.5	5.1×10^{16}	2.8×10^{17}	2.6×10^{16}	3×10^{4}
Y011D	Rev.	1	2340		5.1×10^{16}	2.8×10^{17}	2.6×10^{16}	5×10^{4}
Y012D	Rev.	1	3120		5.1×10^{16}	2.8×10^{17}	2.6×10^{16}	5×10^{4}
Y014D	Rev.	1	1040		5.1×10^{16}	2.8×10^{17}	1.6×10^{17}	6×10^{6}

However, in a current-matched absorber, V_m is smaller at a deeper stage with a thicker absorber. Equation (25) indicates that the dark current will be lower in a multistage device with more stages and thinner individual absorbers; this coincides with the measured dark-current characteristics (Fig. 25). The detector absorbers with λ_{cutoff} near 4.3 μm at 300 K are constructed from InAs/GaSb/(Al, In)Sb/GaSb M-shaped SLs with layer thicknesses of 27, 15, 8, and 15 Å, respectively, for a period of 65 Å [66]. Under the average doping concentration of 2.4×10^{16} cm^{-3}, carrier transport in the absorbers is determined by electrons as minority carriers.

If the detector is reverse biased by high voltage, the carriers are swept out from the absorbers, and then the dark-current density can be calculated by

$$J_d = -qg_{\text{th}}d_1 + \frac{V - J_d R_s A}{R_{\text{shunt}} A}. \tag{26}$$

The dark-current density is dominated by the first-stage contribution (the stage with the thinnest individual absorber). The second term of Eq. (26) takes into account the leakage current density with shunt resistance, R_{shunt}. R_s is the series resistance. A linear dependence between dark-current density and high reverse voltage permits the thermal generation rate and carrier-lifetime extraction assuming the correctness of Eq. (14). The effect of radiative recombination is omitted in Eq. (14), because under near-room-temperature conditions the SRH and Auger recombination mechanisms are predominant.

TABLE III. Summary of design and material parameters for LWIR wafers (based on Ref. [46]).

Wafer	N	GaSb/InAs in a period (Å)	InSb interface (Å)	Number of QWs in electron barrier	Mismatch of SL in growth direction (%)	90% λ_{cutoff} (μm) at 200 K	E_g (meV) at 0 K	E_a[a] (meV) 7–125 K	E_a (meV) 150–250 K	
								q[a] $= 0$	$q = 2$	$q = 1$
S1-8 reg.	8	21.7/35	4.3	3	-0.100	12.8	124	31	51	65
S1-8 rev.	8	21.7/35	4.3	3	-0.390	10.7	144	27	99	118
S2-1	1	22.3/33.9	3.8	3	-0.205	10.2	150	53	73	89
S2-4	4	22.3/33.9	3.8	3	-0.290	9.8	154	62	97	113
S3-1	1	24.7/31	2.1 + 2.2	3	0.111	9.1	164	45	132	148
S3-4	4	24.7/31	2.1 + 2.2	3	0.128	9.3	162	42	124	140
S3-6	6	25.2/31	1.9 + 1.9	3	0.037	9.0	167	39	139	156
S3-8	8	25.2/31	1.9 + 1.9	3	0.043	8.8	171	40	149	166
S4-4	4	25.2/31	1.9 + 1.9	4	0.104	8.8	170	41	154	170
S4-6	6	25.2/31	1.9 + 1.9	4	0.086	8.8	171	44	157	173
S4-8	8	25.2/31	1.9 + 1.9	4	0.092	8.8	174	45	157	173

[a] E_a and q are parameters in the following equation to estimate the temperature dependence of the R_oA product: $R_oA = CT^{-q}\exp(E_a/T)$.

Equation (27) shows the linear dependence of dark-current density versus high reverse voltage:

$$J_d = \left(-qg_{\text{th}}d_1 + \frac{V}{R_{\text{shunt}}A}\right)\Big/\left(1 + \frac{R_s}{R_{\text{shunt}}A}\right), \qquad (27)$$

which is supported by experimental data for five multistage devices in the voltage range between −1.5 and 3.0 V (Fig. 26). The thermal generation rate, g_{th}, at 300 K can be extracted from the intercept of the fitted line with the vertical axis, while the shunt resistance is obtained from the slope of the fitted curve. The series resistance extracted from differential resistance at a high forward voltage is less than 10 Ω at 300 K and is 2 orders of magnitude lower than R_{shunt}. As a consequence, the term R_s/R_{shunt} in Eq. (27) can be ignored.

The minority-carrier lifetime can be calculated with Eq. (14) using the extracted g_{th} value and the intrinsic carrier concentration, n_i. Figure 27 shows the temperature (in the range between 200 and 340 K) dependence of the thermal generation rates and carrier lifetimes at higher reverse bias. The carrier lifetime in the high-temperature range is extracted to be between 8.5 and 167 ns and exhibits a rapid decrease versus temperature. This dependence can be attributed to the Auger *g-r* processes, the contribution of which increases with narrowing of the absorber band gap at high temperature. This behavior is different from previous results obtained using alternative experimental methods following a $1/\sqrt{T}$ law determined by the SRH *g-r* process [67–70].

C. Growth and fabrication of IB QCPs

The IB QCPs contain very complex structures constructed from, in certain cases, thousands of layers. This structure cannot be fabricated using conventional growth techniques, such as CVD or LPE. Only MBE is a reliable layered technique for the fabrication of multistage devices. This sophisticated technique, due to atomic layer-by-layer growth, enables control of molecular (or atoms) beams onto a heated substrate under high vacuum conditions [71,72]. Since the design of multistage devices is relatively complicated, involving many interfaces and strained thin layers, their growth by MBE is challenging.

The MBE systems used in the fabrication of T2SL IB QCP structures are equipped with Sb and As crackers, several effusion cells (In, Ga, Al), and doping cells (typically Si for donor doping and Be for acceptor doping). The MBE systems contain, on average, 10 effusion cells.

Different fabrication procedures are described in the literature. Generally, we can distinguish the following fabrication processes, elaborated by the OU laboratory involved in the development of multistage devices [32]:

(i) standard cleaning;
(ii) mesa etching;
(iii) insulating-layer deposition;
(iv) contact opening;
(v) top-contact deposition;
(vi) lapping;
(vii) bottom-contact deposition;
(viii) mounting and wire bonding.

To define a mesa structure, deep wet etching below the active region is used. Then, for device passivation, about 200-nm-thick SiN_x followed by about 200-nm-thick SiO_2 are deposited by sputtering. Next, on the top of mesa, a window is opened by reactive ion etching. Finally, 30- or 300-nm-thick Ti/Au contact layers are deposited by the sputtering technique. The schematic cross section of the $N = 3$-stage IB QCP is shown in Fig. 28(a). Figure 28(b) shows the cross-section scanning electron microscope image of this device.

The T2SL material system is a natural candidate for realizing multiple-stage IB devices. The photodetector designs exhibit key differences in their approach to construct active and barrier regions, as well as the contact layers. Table I describes the four most popular types of SL barrier detectors, where the material of the active layer or barrier and their doping can be varied. The absence of a conventional depletion layer in barrier photodetectors suppresses the contribution from the depletion current and the SRH *g-r* noise.

Figure 29 shows the general design structure of the two types of T2SL cascade detectors, which can be classified into regular- and reverse-illumination configurations, as shown in Fig. 13. In the regular configuration, photons and electrons travel in the same directions, while, in the reverse configuration, they travel in opposite directions. Fabrication of the two configurations can be realized by reversing the growth order of the layers without changing the light-illumination direction. The reverse configuration is preferred for *p*-type absorbers because photoexcited electrons are more effectively collected.

A single stage of the reverse configuration is similar to a complementary barrier infrared detector (CBIRD) structure (see Table I), in which the absorber (InAs/GaSb T2SLs) is shorter than the diffusion length and is located between an engineered GaSb/AlSb QW EB and an AlSb/InAs QW HB. The design of this structure is shown in Fig. 30 in detail. The electron-relaxation region and the interband-tunneling region also serve as the hole and electron barriers, respectively. The barriers act as a means of leakage-current suppression. The electron-relaxation region is precisely designed to facilitate the extraction of photogenerated carriers from the conduction miniband of the absorber and transport them ideally (with little or no resistance) to the valence band of the absorber in the next stage. As shown, the energy levels of coupled InAs/AlSb multi-QWs in the conduction band form several staircases, with energy-ladder separations comparable to the LO-phonon energy. The uppermost energy

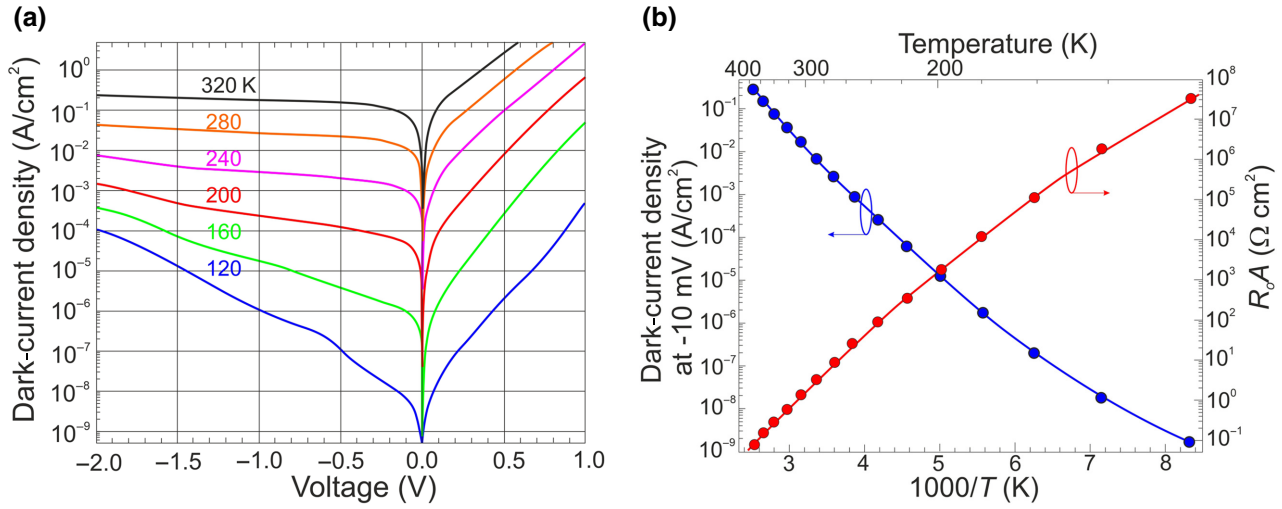

FIG. 31. Dark-current density of $N = 5$-stage MWIR T2SL InAs/GaSb 90-period IB QCP: (a) current-voltage characteristics, (b) Arrhenius plots (based on Ref. [44]).

level of the relaxation-region staircase is close to the conduction miniband in the InAs/GaSb SL, and the bottom energy level is positioned below the valence-band edge of the adjacent GaSb layer, allowing interband tunneling of extracted carriers to the next stage.

As an example, Table II summarizes MWIR wafers ($\lambda_{cutoff} \approx 4.3$ μm at 300 K) with selected numbers of cascade stages and illumination configurations [47]. The absorbers are composed of InAs(27 Å)/GaSb(15 Å)/(Al, In)Sb(8 Å)/GaSb(15 Å) M-shaped SLs for a period of 65 Å [78]. Additional thin Al(In)Sb layers are included in the InAs/GaSb SL to stabilize the influence of layer-thickness fluctuations on the miniband energy. The EB has four GaSb/AlSb QWs with GaSb QW widths of 33, 43, 58, 7, and 3 Å, while the HB is made of seven digitally graded InAs/AlSb QWs with InAs QW thicknesses of 33.5, 36.5, 40.5, 45.5, 52, 59, and 68 Å.

Similarly to Table II, Table III presents the design and material parameters for LWIR wafers. The 90% λ_{cutoff} of the fabricated photodetectors is between 7.5 and 11.5 μm within a temperature range of 78 to 340 K. The composition of the SL periods is slightly adjusted by InSb interfaces, as indicated in the table. An approach to divide a thick InSb layer at the GaSb-on-InAs interface (see the first four wafers in Table III) into thinner InSb layers is used to achieve strain balance in the SL detectors for the LWIR region [79]. It appears that the interface quality is reasonably controlled and allows the fabrication of photodetectors with good performance. Moreover, the incorporation of an InSb interfacial layer into the InAs/GaSb T2SL allows the minority-carrier lifetime to be increased [80].

The next two sections present the performance of high-quality IB QCPs operating in the MWIR and LWIR regions. Experimental data are mainly taken from two research groups guided by Yang (OU) and Krishna (University of New Mexico and Ohio State University).

V. MWIR INTERBAND QUANTUM CASCADE PHOTODETECTORS

Figure 31 shows the dark-current-density temperature dependence of the 90-period MWIR IB QCP. The low-temperature J-V curves are fairly steep [see Fig. 31(a)], which indicates the tunneling-component contribution. At higher temperatures, the dark current is much less sensitive to the voltage and is diffusion limited.

The analyzed $N = 5$-stage detectors are grown by MBE on Zn-doped 2″ (001) GaSb substrates. The absorbers are composed of p-doped ($\sim 5 \times 10^{15}$ cm^{-3}) T2SL InAs/GaSb with InSb interfacial layers to balance strain introduced by the lattice-mismatched InAs. The V/III beam-flux ratios for Sb/Ga and As/In are assumed to be 4 and 3.2, respectively. The detectors consist of a 0.5-μm-thick p-type GaSb buffer layer, $N = 5$-stage IB QCP equal-absorber structure, and finally a 45-nm-thick n-type InAs top-contact layer. The individual absorbers consist of 30, 60, and 90 periods of InAs(7 ML)/GaSb(8 ML) T2SLs, which correspond to net absorber thicknesses of 0.73, 1.45, and 2.16 μm, respectively. Single-pixel circular mesa-sized devices (ranging from 25 to 400 μm in diameter) are analyzed. A 200-nm-thick SiN_x film is deposited for sidewall passivation. Top and bottom contacts are formed by e-beam evaporated Ti/Au. No antireflection coating is applied.

Further information on dark-current curves is given by the Arrhenius plot at −10 mV and zero-bias resistance-area product (R_oA) [see Fig. 31(b)]. The activation energy (E_a) under HOT conditions is about 0.302 eV,

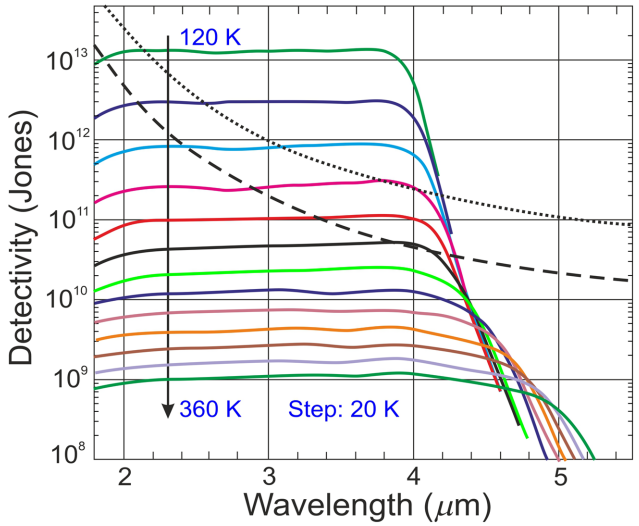

FIG. 32. Johnson-noise-limited D^* for $N = 5$-stage MWIR T2SL InAs/GaSb 90-period IB QCP for selected temperatures (based on Ref. [44]). Dashed lines represent the BLIP D^* for a photovoltaic detector with an external QE of 70%, and dotted lines are the BLIP D^* for $N = 5$-stage device with an absorption QE of 70%, both at 300 K background with 2π field of view (FOV).

which is very close to the T2SL InAs/GaSb active-layer effective band gap, proving the diffusion-component contribution. The R_oA product exceeds 1.25×10^7 $\Omega\,\mathrm{cm}^2$ (at 120 K), 2470 $\Omega\,\mathrm{cm}^2$ (at 200 K), and 3.93 $\Omega\,\mathrm{cm}^2$ (at 300 K). The dark-current density reaches about 1.28×10^{-7} A/cm^2 at 160 K, and the extracted $R_oA \sim 9.42 \times 10^4$ $\Omega\,\mathrm{cm}^2$ is slightly better than the (Hg, Cd)Te "Rule 07" [81].

The spectral responsivity of the MWIR T2SL IB QCP reaches about 0.3 A/W at $T = 300$ K and $\lambda = 4$ μm and is measured up to 380 K. Figure 32 presents the Johnson-noise-limited D^* at selected temperatures, to assess the measured responsivity and R_oA. The Johnson-limited D^* reaches about 1.29×10^{13} cm Hz$^{1/2}$/W at 3.8 μm and 120 K and 9.73×10^{11} cm Hz$^{1/2}$/W at 200 K. The background limited infrared photodetector (BLIP) performance reaches 180 K at 4 μm for $N = 5$ stages per junction devices with 70% absorption QE, corresponding to 14% external QE.

Equation (6) and experimental data for $R_i \approx 0.3$ A/W allow the room-temperature conversion QE at $\lambda = 4$ μm to be estimated as $\eta g \approx 9\%$. The gain is estimated at the level of $g = 0.2$, leading to the absorption QE of 45%. The absorption QE will increase versus the number of stages provided that the absorbers are not very thick, ensuring equal absorption of the photon flux at each stage (total thickness of all stages should be comparable to the diffusion length). However, the conversion QE remains lower than that of the absorption QE by a factor of the number of absorbers (stages).

Figure 33 presents the response time of an IB QCP versus temperature at zero bias [see Fig. 33(a)] and versus voltage for $T = 225$, 293, and 380 K [see Fig. 33(b)]. These results confirm the short response time of IB QCPs. At zero bias, within the temperature range of 225–280 K, the response time increases with temperature from about 1 to 5 ns. It stabilizes at about 5 ns for further increases in temperature to about 360 K, then it decreases, reaching about 2 ns at 380 K.

As shown in Fig. 33(b), the reverse voltage is beneficial for the IB QCP response time. The negative correlation between the response time and bias for temperatures of 225 and 293 K is probably related to the drift-component decrease versus voltage as the electric field drop increases across the absorber region. In this context, the behavior of the response time versus bias above 200 mV and $T = 380$ K is not fully understood as the time response increases with voltage. It is believed that, under this condition, separation of the quantized energy in the tunneling region and the valence band in the transport region does not match the LO-phonon energy in AlSb, which is responsible for the tunneling of holes through a phonon-assisted process. In addition, ambipolar mobility is reduced, which, in turn, influences the detector's time response.

The photoexcited carriers are transported very rapidly over a distance in the cascade that is much shorter than the diffusion length (approximately 50–200 nm, depending on wavelength). Since lateral diffusion transport is not significant, there is no need to implement the deeply etched mesa structures for confining photoexcited carriers in QCPs, in comparison with conventional photodiodes. In addition, high wave-function overlap in the relaxation region causes the IS relaxation time (e.g., optical-phonon scattering time, $\sim$1 ps) to be much shorter than the IB recombination time ($\sim$1 or $\sim$0.1 ns under HOT conditions with significant Auger g-r); this allows the photoexcited electrons to be efficiently transferred to the bottom of the energy ladder.

Lei *et al.* reported a comparison study of different MWIR IB QCPs, where the number of cascade stages, absorber thicknesses, and doping concentrations were changed [47]. Table IV gathers the performance of devices at 300 K made from the wafers summarized in Table II. Carrier transport in photodetectors made from wafers highlighted in Table II wafers is dominated by diffusion current near room temperature. However, their current density-voltage characteristics are sensitive to device size, which is probably due to imperfect passivation.

Figure 34 presents the dynamic RA product, current responsivity, and detectivity versus voltage for a photodetector fabricated from the R146 wafer (see Table II), operating at 300 K and $\lambda = 3.3$ μm. Due to significant surface-leakage current, the value of the RA product is lower than expected, and the detectivity is about 10^9 cm Hz$^{1/2}$/W. At zero bias, the detectivity is limited by Johnson noise, while, under reverse bias, D^* is influenced

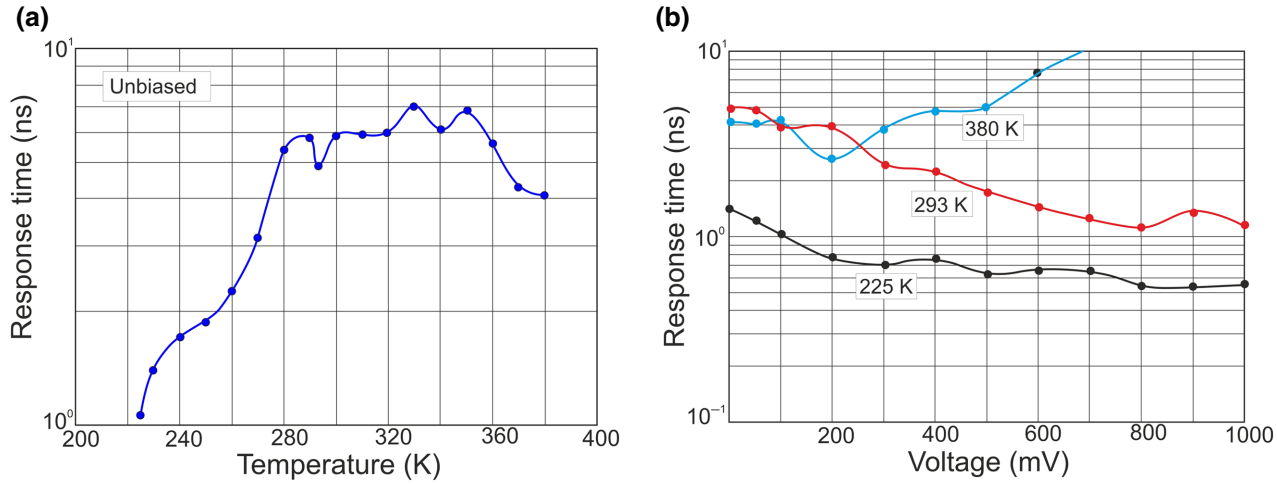

FIG. 33. T2SL MWIR IB QCP response time: (a) at zero bias versus temperature and (b) versus voltage at 225, 293, and 380 K (based on Ref. [43]).

by both Johnson and shot noise. However, the detectivity increases versus reverse bias because the shot noise increases more slowly than the dynamic *RA* product.

Analysis of the temperature and bias dependence of photodetector responsivities with various absorber thicknesses indicates that the diffusion length is between 0.6 and 1.0 μm for T2SL absorbers in the temperature range above 250 K.

As described in Sec. III, the QE for the matched-absorber IB QCPs is equal in each stage and then

$$\eta = (1-r)\exp[-\alpha(d_1 + d_2 + \ldots + d_{N-1})(1 - e^{-\alpha d_N})], \tag{28}$$

where α is the absorption coefficient, r is the reflectance at the top device's surface, and d_N is the absorber thickness for N stages. Alternatively, in the equal-absorber device, the QE is limited by the photocurrent in the last stage, and then

$$\eta = (1-r)\exp[-\alpha(N-1)d](1 - e^{-\alpha d}). \tag{29}$$

However, if the electric gain is not unity, $g \neq 1$, the current responsivity can be given by

$$R_i = \frac{q\eta\lambda}{hc} g = (1-r)\frac{q\lambda}{hc} g(1 - e^{-\alpha d_1}), \tag{30}$$

where λ is the wavelength, h is Planck's constant, and c is the speed of light.

Equations (29) and (30) allow the electric gain to be estimated from experimentally measured absorption coefficients and current responsivities. The absorption coefficient for MWIR devices is 3100 cm^{-1} at 3.3 μm [47]. Figure 35 shows the extracted electric gain for multistage photodetectors operating at room temperature and fabrication of the wafers presented in Table II. As shown, the electric gains are between 1.2 and 1.6 for matched-absorber devices and a one-stage detector. The highest gain, $g \sim 2$, is reached for an 8-stage equal-absorber photodetector with very thin absorbers (312 nm).

The $N = 5$-stage MWIR IB QCPs described by Tian and Krishna are used to demonstrate the first 320×256 focal-plane array (FPA) with pixel sizes of 24×24 μm^2 and a pitch size of 30 μm [44,82]. The diced FPAs are hybridized to Indigo read-out integrated circuits. The minimum noise-equivalent temperature difference of 28 mK is reached at 120 K. This device exhibits a BLIP performance above 150 K (300 K, 2π FOV). Generally, however, the performance is worse than that of current T2SL-barrier-detector FPAs [39].

VI. LWIR INTERBAND CASCADE PHOTODETECTORS

Research into LWIR and VLWIR IB QCPs with $\lambda_{cutoff} \leq 16$ μm at 78 K is presented in several papers [35,45,46,79,83].

Figure 36 shows the $N = 2$-stage LWIR device grown by MBE. The absorber layers are 620.0 and 756.4 nm thick with T2SLs constructed from 36.3-Å InAs and 21.9-Å GaSb, where 1.9-Å-thick InSb is introduced into both InAs-on-GaSb and GaSb-on-InAs as the interface strain-balancing layer. The deeper absorber is grown thicker to reach current matching. To make electrons the minority carriers, half of the T2SL GaSb absorbers are p doped to the level of 3.5×10^{16} cm^{-3}. Both EB and HB have identical designs. Square mesa devices with edge lengths ranging from 200 to 1000 μm are fabricated. 170-nm-thick Si_3N_4 followed by 137-nm SiO_2 are used for two-layer passivation.

TABLE IV. IB QCP performance at $\lambda = 3.3\ \mu$m (background $T = 25$ °C, FOV $= 2\pi$) at 300 K (based on Ref. [47]).

Detector	R146	Y004D	Y005D	Y008D	Y009D	Y007D	Y010D	Y014D	Y011D	Y012D
Number of stages	8	3	3	6	8	3	1	1	1	1
100% λ_{cutoff} (μm)	4.3	4.3	4.3	4.3	4.3	4.3	4.2	4.4	4.4	4.5
Device dimension (mm)	0.20	0.40	0.40	0.50	0.20	0.40	0.20	0.10	0.20	0.20
Zero-bias D^* (Jones)	9.7×10^8	1.3×10^9	1.1×10^9	1.5×10^9	1.1×10^9	1.6×10^9	1.6×10^9	1.0×10^9	1.3×10^9	1.0×10^9
R_i (A/W)	0.13	0.24	0.21	0.20	0.15	0.31	0.67	0.64	0.84	0.71
R_oA (Ω cm^2)	0.96	0.46	0.51	0.93	0.86	0.42	0.089	0.042	0.041	0.036
D^* under bias (Jones)	1.2×10^9	1.5×10^9	1.4×10^9	1.8×10^9	1.3×10^9	1.8×10^9	1.9×10^9	1.2×10^9	2.1×10^9	2.0×10^9
	(−500 mV)	(150 mV)	(150 mV)	(200 mV)	(400 mV)	(150 mV)	(150 mV)	(100 mV)	(100 mV)	(100 mV)
J_d (A/cm^2) under bias	0.26	0.17	0.15	0.17	0.26	0.23	0.45	0.87	1.13	1.52
R_i (A/W) under bias	0.14	0.24	0.23	0.20	0.16	0.35	0.74	0.64	1.30	1.48
RA (Ω cm^2)	4.41	2.03	2.67	2.98	2.97	1.17	2.16	0.48	0.35	0.18

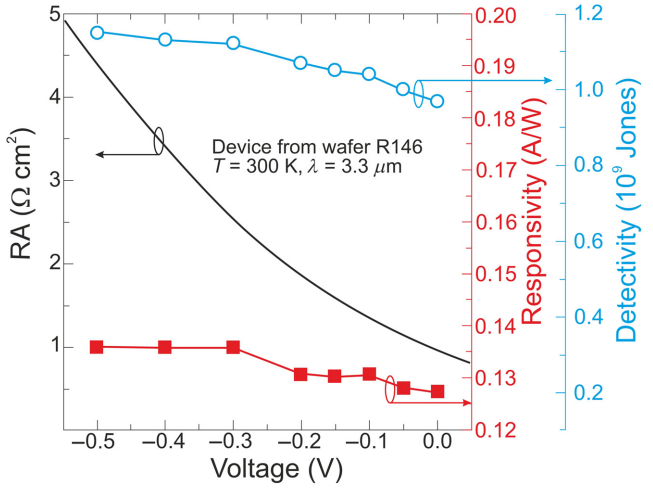

FIG. 34. Dynamic RA product, current responsivity, and detectivity versus voltage for a photodetector fabricated from the R146 wafer (see Table II) at 300 K (based on Ref. [47]).

Dark-current density curves versus voltage for selected temperatures (78–250 K) are shown in Fig. 37 [45]. E_a is estimated to be 102 meV (see inset) in comparison with the corresponding value of $E_g \sim 135$ meV at 78 K, which indicates that the detector is limited by neither diffusion nor the g-r process ($E_a > E_g/2$). Nonuniform doping in the absorber region creates an electric field that influences the SRH g-r and leads to deviations in the diffusion-limiting operation. Unintentional electrostatic barriers also lead to a lower collection efficiency due to ineffective hole transport in the active layers (n-type under HOT conditions) and external bias is required to increase the collection of photocarriers.

Figure 38 shows the Johnson-limited D^* of LWIR IB QCPs at selected temperatures (78–220 K). At

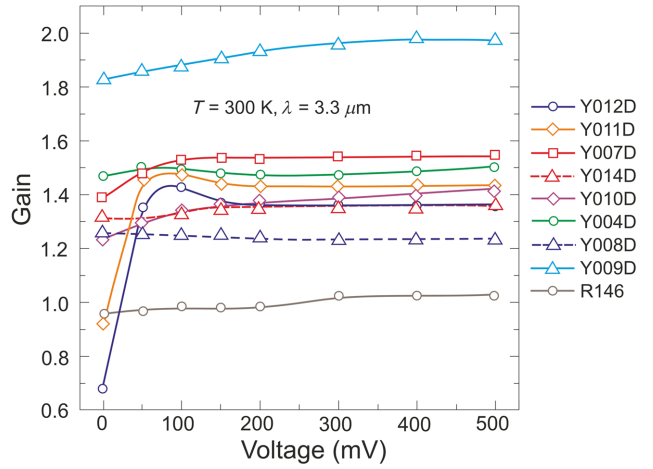

FIG. 35. Extracted electric gain at 3.3 μm for devices fabricated from wafers (see Table II) at 300 K (based on Ref. [47]).

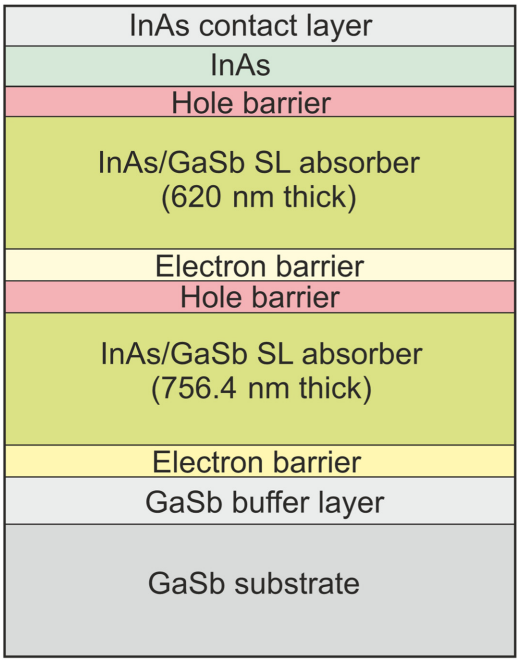

FIG. 36. Device structure for $N = 2$-stage LWIR IB QCP (based on Ref. [45]).

78 K, $R_oA \sim 115\ \Omega\,\text{cm}^2$, corresponding to $D^* \sim 3.7 \times 10^{10}\ \text{cm}\,\text{Hz}^{1/2}/\text{W}$ at 8 μm.

Comparative studies of different sets of LWIR IB QCPs based on T2SLs have been undertaken by the research group at OU [46,83]. Both equal-absorber and matched-absorber photodetectors with regular- and reverse-illumination configurations are considered. Table V gathers the material properties and designs of four devices with λ_{cutoff} in the 8–12 μm spectral range.

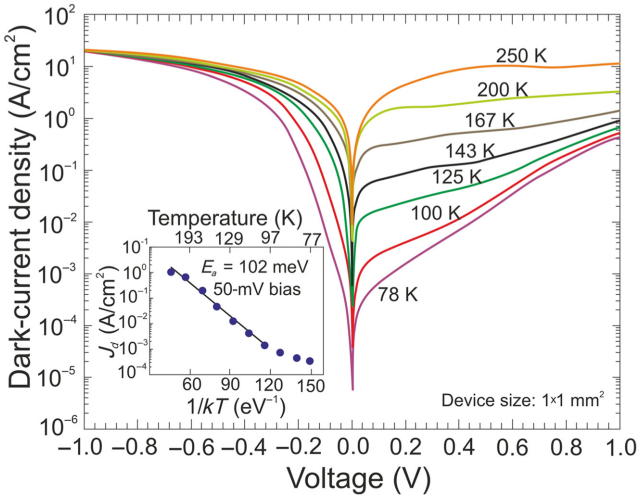

FIG. 37. Current-voltage dark-density curves at selected temperatures for LWIR detector. Inset shows the fitted activation energy for the Arrhenius plot (based on Ref. [45]).

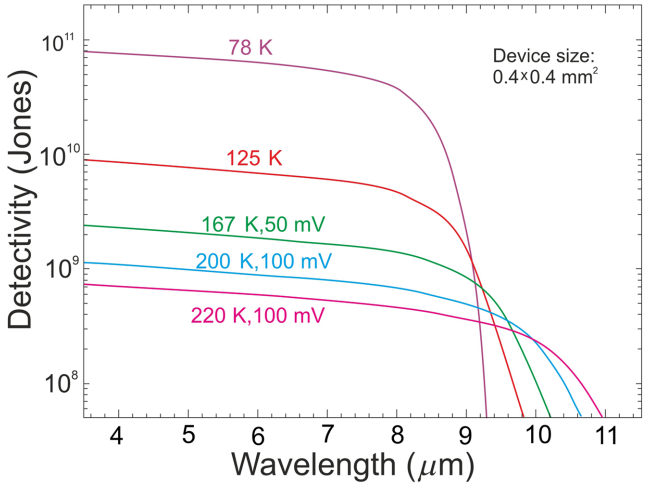

FIG. 38. D^* of LWIR IB QCP for temperatures of 78–220 K (based on Ref. [45]).

The temperature dependences of the R_oA products shown in Fig. 39 are extracted from the dark-current–voltage (J_d-V) characteristics. Arrhenius plots indicate that there are low- and high-temperature regions with proper linear fits and two separate activation energies: one for the low-temperature range of 78–125 K and the other for the high-temperature range of 150–250 K. At high temperature, carrier transport is diffusion limited with an activation energy, E_a, similar to the band gap at zero temperature. However, the activation energies at lower temperature (78–125 K) are far below the band gaps, which suggests the contribution of TAT [46].

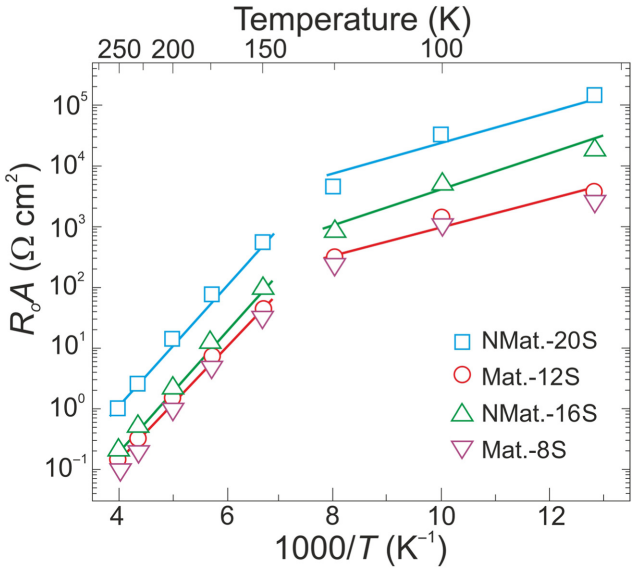

FIG. 39. Extracted R_oA product versus temperature for devices given in Table V (based on Ref. [83]).

TABLE V. Summary of material and design parameters for LWIR IB QCPs (based on Ref. [83]).

Device	Absorber type	Number of stages	Total absorber thickness (μm)	100% λ_{cutoff} (μm) at 300 K	E_g (meV) at 0 K	E_a (meV) 78–125 K	E_a (meV) 150–250 K
NMat.-20S	Identical	20	3.60	9.5	188	43	160
Mat.-12S	Current matched	12	4.44	11.0	174	45	155
NMat.-16S	Identical	16	3.55	11.1	172	64	160
Mat.-8S	Current matched	8	2.29	11.0	175	45	155

As shown by Eq. (18), the R_oA product is proportional to the sum of $1/\tanh(d_m/L_m)$. This means that, for detectors with thicker absorbers, the R_oA product is lower, but, for detectors with more stages, the R_oA product is higher. This behavior is supported by experimental data (Fig. 39 and Table V).

Figure 40 presents the current responsivities of the samples given in Table V. As shown, the four devices exhibit similar trends, with responsivities increasing versus temperature, reaching a maximum at certain temperatures and then decreasing. The diffusion length, above 0.5 μm at 300 K, is longer or comparable to the thicknesses of the absorbers, which means that photocarrier collection does not affect the characteristics of devices at various temperatures. Consequently, the increase of R_i versus temperature is conditioned by an increase of the absorption coefficient due to narrowing of the band gap at higher temperatures. However, in the higher-temperature range, the responsivities decrease as a consequence of more considerable attenuation of radiation in the deeper stages. The last effect is more significant for devices with thicker absorbers. Comparing the two sets of devices (equal and matched absorbers), the current-matched (matched absorbers) devices present higher responsivities and correlation of reduced responsivity with radiation attenuation in deeper stages.

The current responsivity for equal-absorber (non-current-matched) and matched-absorber (current-matched) devices can be described by

$$R_i = (1-r)\frac{q\lambda}{hc}gexp[-\alpha(N-1)d](1-e^{-\alpha d}), \qquad (31)$$

and Eq. (30), respectively. Taking into account the measured values of absorption coefficients and current responsivities, electric gain can be extracted using Eqs. (30) and (31), as shown in Fig. 41 for two devices [83]. The behavior of electric gain depends on the type of device. If the absorption coefficient is higher than about 1000 cm^{-1}, the electric gain exceeds $g > 1$; however, with further increasing α, the electric gain for current-matched devices remains nearly constant, whereas, for equal-absorber structures, the gain increases. Strong absorption in the region of large photon energy causes significant attenuation of the radiation intensity in the last stage and large electric gain is required to maintain current continuity. To fulfil the current-continuity requirement, the electric gain should

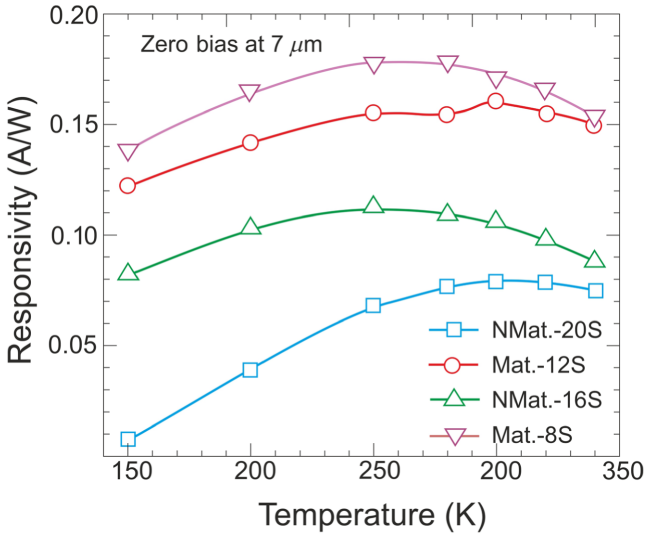

FIG. 40. Dependence of current responsivity on temperature for samples given in Table V (based on Ref. [83]).

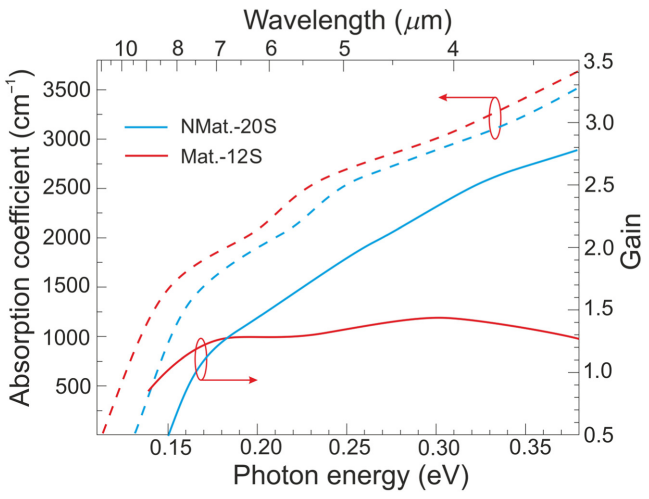

FIG. 41. Absorption coefficient and electric gain at room temperature for two samples given in Table V (based on Ref. [83]).

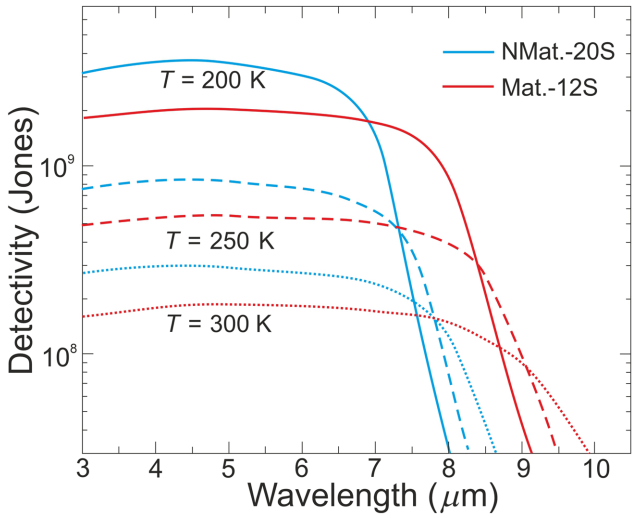

FIG. 42. Johnson-noise-limited detectivity at 200, 250, and 300 K for two devices given in Table V (based on Ref. [83]).

be higher in devices with thinner absorbers to compensate for a shorter absorption length. In general, the electric gain can offset radiation attenuation at a deeper stage. The significantly higher R_oA product (see Fig. 39) and suppressed noise for equal-absorber (not-current-matched) devices result in detectivity comparable to that of current-matched ones. Summarizing, perfect current matching for multistage devices is not necessary. This conclusion permits greater flexibility in the design and implementation of IB QCPs.

Figure 42 shows the estimated zero-biased Johnson-noise-limited detectivities based on the measured R_oA products and current responsivities [83]. The highest D^* value is presented by the equal-absorber device with more stages ($N = 20$). At room temperature, the corresponding values are about 2×10^8 cm Hz$^{1/2}$/W, which exceed the reported values for commercially uncooled (Hg, Cd)Te detectors [84]. In terms of detectivity, both sets of devices (not-current and current-matched) have comparable performances.

LWIR IB QCPs are capable of operating at temperatures as high as 340 K, while MWIR IB QCPs are reported to operate at 420 K [42,46]. Additionally, in the high-temperature region, negative differential conductance (NDC) is observed. NDC is related to intraband tunneling through the EB.

For a standard double-barrier resonant tunneling diode (RTD), as shown in Fig. 43(a), a QW is sandwiched between two heavily n-doped regions. At equilibrium, the QW's ground-state energy is located above the Fermi level in the two adjacent regions. As the device is biased, the QW's level aligns with the filled states in one n-type region (the emitter) above the conduction band and below the Fermi level. In the opposite n-type region (the collector), the Fermi level is moved further down by the voltage, such that empty states above the Fermi level are in line with the QW's ground state. Accordingly, the electrons resonantly tunnel through the QW from the occupied states on one side of the double barrier to the empty states on the other, which results in the current increasing. Further biasing causes a drop of the QW's ground state below the conduction band of the emitter, and there are no longer occupied states able to provide electrons for the tunneling process. This causes a decrease in current with increasing voltage, leading to NDC. The left part of Fig. 43(a) shows the three key bias regions described above for a RTD.

Similarly to the RTD, for the biased IB QCP, the multiple QW ground energies align such that electrons in the HB region can tunnel into the conduction band of the absorbing region in the next stage. Figure 43(b) shows the effect of biasing on IB QCPs and the resonant tunneling effect. As shown, resonant tunneling occurs through the stage barriers for high voltages [85]. Figure 44 presents

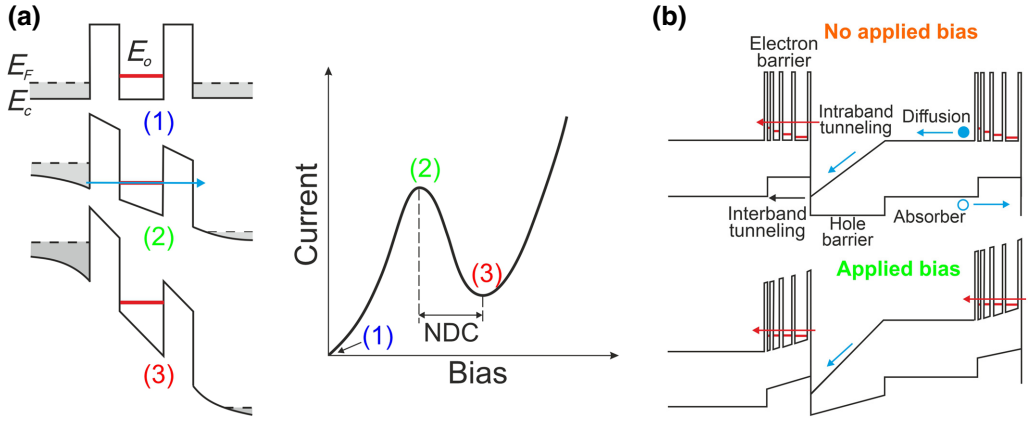

FIG. 43. Resonant tunneling through the multi-QW EB: (a) energy-band diagrams of resonant tunneling, (b) resonant tunneling in a multistage IB QCP (based on Ref. [85]).

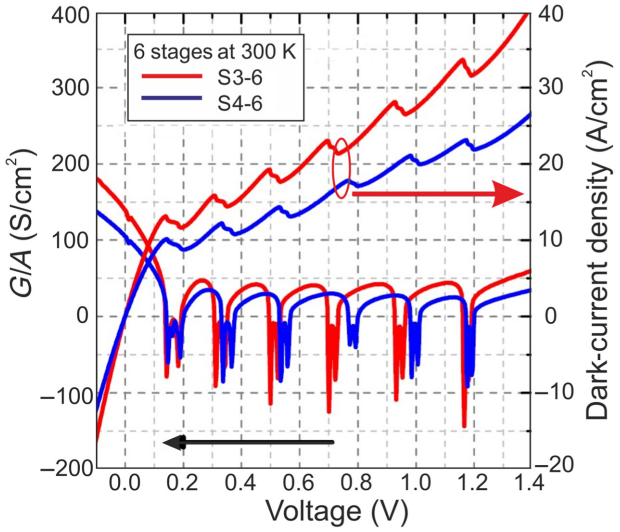

FIG. 44. Ratio of differential conductance to area and dark-current density versus voltage for $N = 6$-stage IB QCP (based on Ref. [46]).

differential current-voltage characteristics of the $N = 6$-stage IB QCP. The NDC peaks are observed, where the number of peaks corresponds to the number of stages.

To improve the LWIR T2SL QCP's performance, further improvements in device technology and design are needed, such as shorter active layers and better band-gap alignments between the absorbers and the EB/HB, active-layer p-type doping, and better processing.

VII. PERFORMANCE COMPARISON WITH (Hg, Cd)Te HOT PHOTODETECTORS

In 2007, Teledyne published Rule 07, an empirically derived formula, for dark-current assessment of the p-on-n (Hg, Cd)Te photodiodes versus normalized wavelength-temperature product ($\lambda_{cutoff}T$) [81]. Rule 07 is closely related to the Auger-1 diffusion-limited photodiode with n-type extrinsic doping concentration in the active region close to about 10^{15} cm^{-3} and predicts the dark-current density within a factor of 2.5 over a range of 13 orders of magnitude. This formula is popular within the IR community as a reference level (especially for $A^{III}B^{V}$ barrier and T2SL devices). It must be stressed that, the current fabricated fully depleted background-limited (Hg, Cd)Te photodiodes exhibit 300-K dark current, which is significantly lower than that given by the benchmark Rule 07.

A. Law 19

Figure 45(a) shows the band diagram for a reverse P-i-N photodiode. The absorber consists of an undoped i region sandwiched between wider-band-gap P and N regions [see Fig. 45(b)]. For the P-i-N (Hg, Cd)Te photodiode, very low doping in the absorber region ($<5 \times 10^{13}$ cm^{-3}) is required to reach full depletion at zero or low reverse bias [86,87]. The adjacent wide-gap contact layers limit dark-current generation from those regions and the tunneling current under reverse bias. The P-i-N design theoretically suppresses $1/f$ and random telegraph noise, which is compatible with the small pixel size exhibiting low crosstalk (built-in vertical electric field) [88,89].

The SRH g-r carrier lifetime is reported within the range of 0.5–10 ms for low doping of (Hg, Cd)Te (approximately 10^{13} cm^{-3}) grown by MBE, which indicates that the current is suppressed and the performance is limited by background radiation, as presented in Fig. 46 for four background temperatures: 300, 200, 100, and 50 K.

In the *Extended Abstracts* of *The 2019 U.S. Workshop on the Physics and Chemistry of II-VI Materials*, it was proposed to replace Rule 07 with "Law 19," corresponding exactly to the 300-K background-limited curve (see Fig. 46) [86]. The current can be several orders of magnitude below Rule 07 versus λ_{cutoff} and operating T. Rule 07 corresponds to a theoretically predicted curve for an Auger-limited p-on-n photodiode with a doping concentration in the active region equal to $N_d = 10^{15}$ cm^{-3} (see Fig. 46).

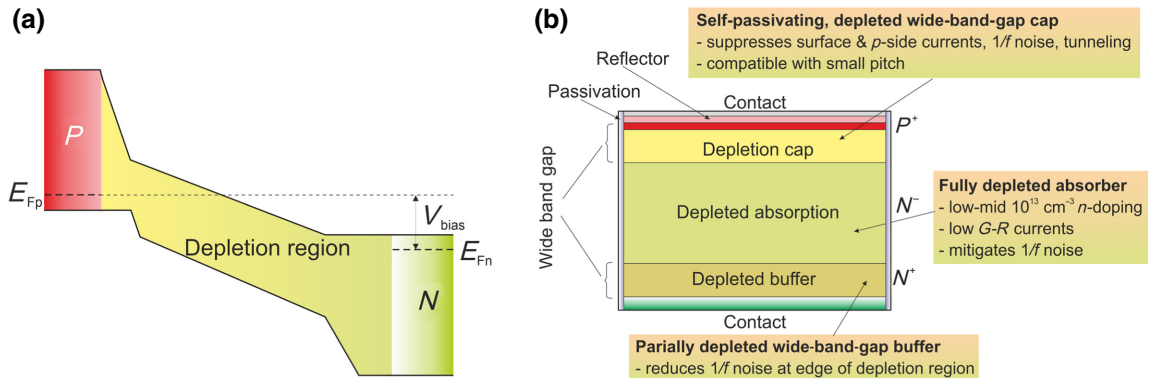

FIG. 45. P-i-N photodiode: (a) band diagram under reverse voltage, (b) P-i-N structure (based on Ref. [87]).

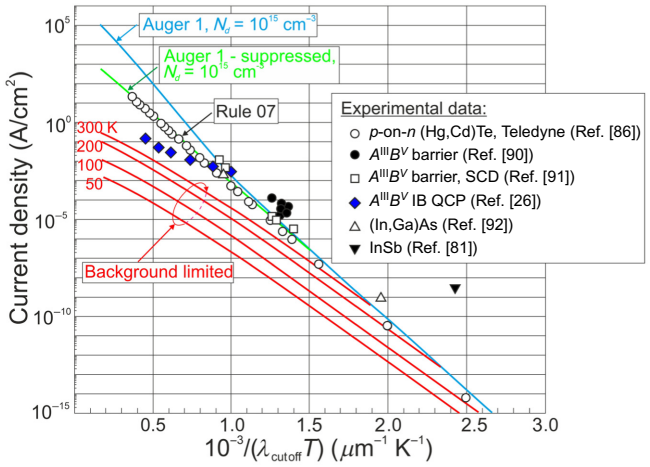

FIG. 46. Current density of p-on-n (Hg, Cd)Te photodiodes versus $1/(\lambda_{cutoff}T)$ product (based on Refs. [26,81,86,90–92]). Experimental data are gathered for Teledyne and alternative technologies.

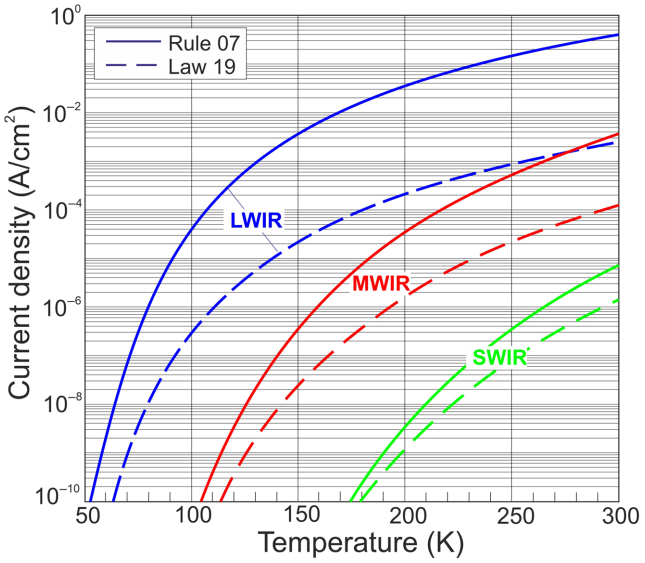

FIG. 47. Calculated current density versus temperature based on Law 19 and Rule 07 for SWIR (λ_{cutoff}= 3 μm), MWIR (5 μm), and LWIR (10 μm) (Hg, Cd)Te absorbers.

Theoretical simulations presented in Fig. 46 show that the background limit has the most impact on the photodiode's current density for small $1/(\lambda_{cutoff}T)$ products for devices operating under LWIR and HOT conditions. (Hg, Cd)Te photodiodes operating at low temperature are g-r limited due to the influence of SRH centers exhibiting lifetimes in the millisecond range.

Figure 47 shows the current density calculated by Rule 07 (for diffusion-limited p-on-n photodiodes) and Law 19 (equal to the background-radiation current density) versus temperature for SWIR (λ_{cutoff}= 3 μm), MWIR (5 μm), and LWIR (10 μm) absorbers.

B. IB QCPs versus (Hg, Cd)Te photodiodes

Figure 48 presents the theoretical predictions of the R_oA product for (Hg, Cd)Te photodiodes versus λ_{cutoff} at 200, 250, and 300 K. In addition, this figure compares the extracted experimental R_oA products for (Hg, Cd)Te photodiodes and IB QCPs based on the T2SL InAs/GaSb absorbers at T = 300 K. It is evident that, at the present level of development of multistage detector technology, the experimentally measured R_oA values at room temperature are higher than those for state-of-the-art (Hg, Cd)Te photodiodes.

The measured peak current responsivities at room temperature for the considered devices, (Hg, Cd)Te photodiodes and IB and IS QCPs, are presented in Fig. 49. The highest responsivity is presented by (Hg, Cd)Te photodiodes, which is mainly caused by high QE, typically about 70%. The peak R_i is generally higher for IB QCPs than that for IS QCPs. The lower responsivity for IS devices is attributed to a much shorter carrier lifetime. An additional contribution can be observed by the polarization selection rule for IS transitions in conduction bands (this effect prohibits normal absorption of radiation).

Figure 50 (dashed and dotted lines) demonstrates that bipolar devices based on T2SL InAs/GaSb IB absorbers are the proper candidates for detectors operating near room temperature. The estimated Johnson-noise-limited detectivities under zero bias for IB QCPs with T2SL InAs/GaSb

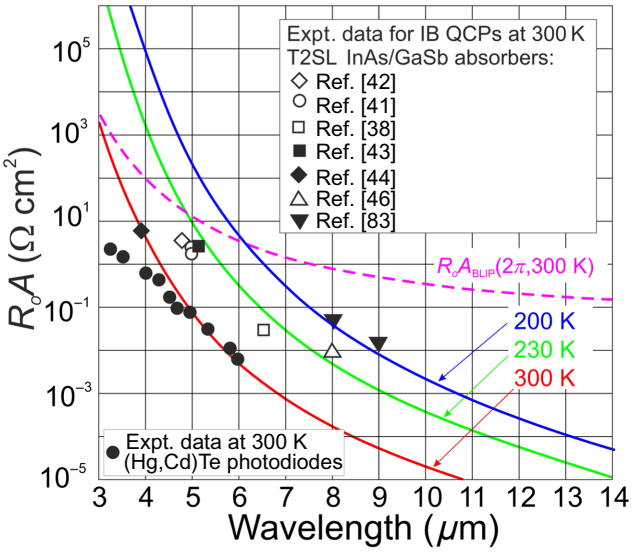

FIG. 48. (Hg, Cd)Te photodiode R_oA products (solid lines) in comparison with room-temperature experimental data for IB QCPs based on T2SL InAs/GaSb absorbers (based on Refs. [38,41–44,46,83]).

absorbers (based on the measured R_oA product and responsivity) are comparable with those for commercially available (Hg, Cd)Te photovoltaic detectors. We can see that the performances of both types of detector are similar in the SWIR region, but IB QCPs outperform commercially available uncooled (Hg, Cd)Te detectors with a similar LWIR λ_{cutoff}. In addition, due to strong covalent bonding of $A^{III}B^{V}$ semiconductors, IB QCPs can operate at temperatures up to 420 °C (MWIR range), which is not possible to reach with the (Hg, Cd)Te counterpart.

Figure 50 also shows the future trend in HOT IR photodetector development. Currently, the semiempirical Rule 07 for (Hg, Cd)Te technology is found not to meet primary expectations. It is shown that D^* of low-doping *P-i-N* (Hg, Cd)Te (approximately 10^{13} cm^{-3}) devices, operating at 300 K for $\lambda > 3$ μm, is limited by background radiation (with $D^* > 10^{10}$ cm Hz$^{1/2}$/W), not limited by detector itself, and can be improved more than 1 order of magnitude in comparison with that predicted by Rule 07. Among materials used for HOT LWIR photodetector fabrication, only (Hg, Cd)Te can meet required expectations: low doping concentration of 10^{13} cm^{-3} and a high SRH carrier lifetime above 1 ms. It will be difficult for IB multistage photodetectors to compete with (Hg, Cd)Te photodiodes. The above-presented estimates encourage the fabrication of low-cost and high-performance MWIR and LWIR (Hg, Cd)Te FPAs operating under HOT conditions. The performance of T2SL IB QCPs is close to that of (Hg, Cd)Te photodiodes and IB QCPs can operate in temperatures above 300 K.

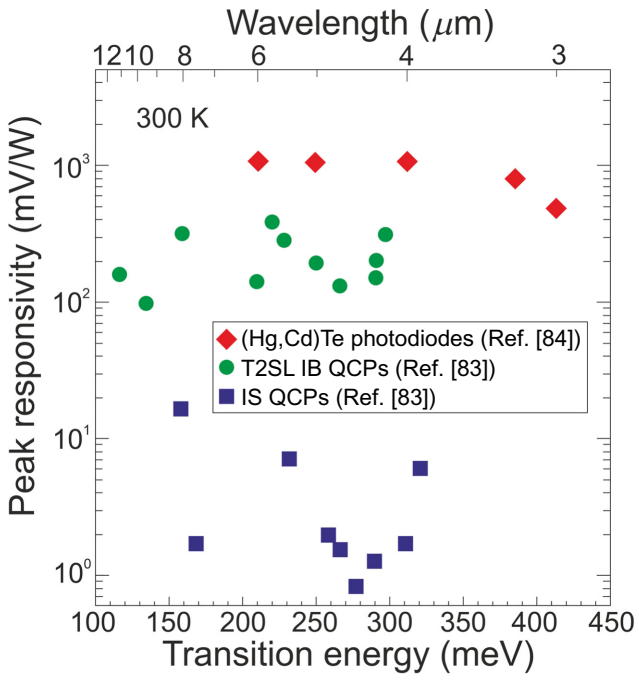

FIG. 49. Measured peak current responsivities for (Hg, Cd)Te photodiodes and IB and IS QCPs at 300 K (based on Refs. [83, 84]).

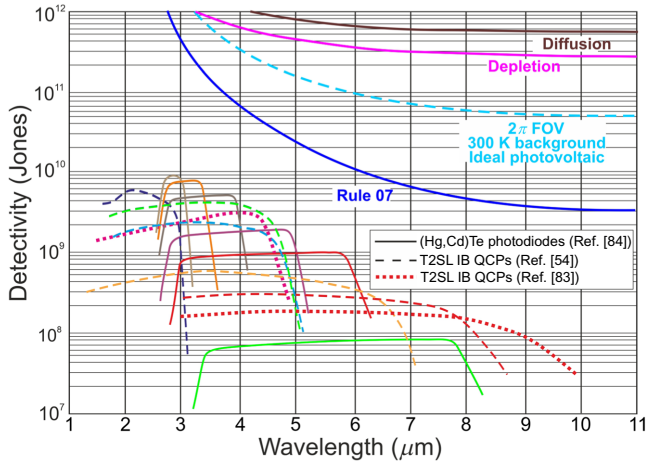

FIG. 50. Room-temperature spectral detectivity curves of commercially available (Hg, Cd)Te photodiodes (solid line) and T2SL IB QCPs (dashed and dotted lines). Adapted from Refs. [54,83,84].

Figure 51 shows the measured response times of the T2SL IB QCP and (Hg, Cd)Te photodetectors (mainly photodiodes) operating within the temperature range of 220–300 K. Most of the zero-biased LWIR photodiodes are characterized by response times below 10 ns. The device response time decreases under reverse bias, reaching <1 ns, which is shorter for T2SL IB QCPs than that for (Hg, Cd)Te photodetectors.

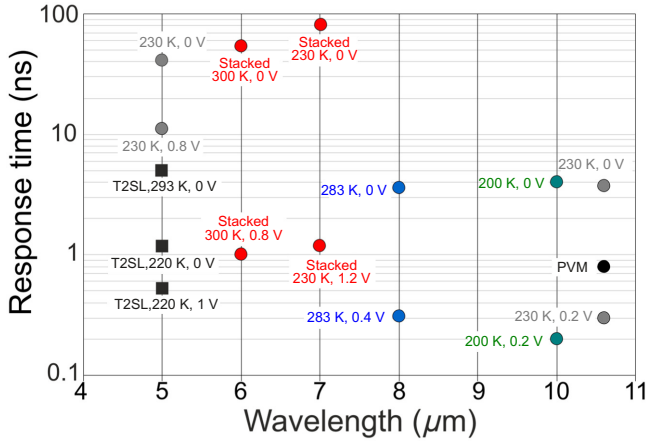

FIG. 51. Response time versus wavelength for unbiased and reverse-voltage (as indicated) (Hg, Cd)Te photodiodes and T2SL MWIR IB QCPs operating in the temperature range between 220 and 300 K. "Stacked," double-stacked photovoltaic detector; PVM, multiple-heterojunction photovoltaic detector (based on Ref. [43]).

C. Interband versus intersubband QCPs

Fundamentally, IB QCPs differ substantially from IS ones (both lasers and detectors), taking into account the activation processes and carrier lifetimes, as discussed in Sec. II C. The carrier lifetime is in the nanosecond range for IB devices and in the picosecond range for IS devices. Usually, the reverse dark-current density approaches a constant value (saturation current, J_o), which is proportional to carrier concentration and inversely proportional to carrier lifetime. Consequently, the dark-current density is at least an order of magnitude lower in IB devices than that in IS devices, as shown in Fig. 8. Similar behavior is observed for the saturation current density (Fig. 9).

Considering that $D^* \sim \sqrt{R_oA}$ and $R_oA = kT/qJ_o$, the detectivity is inversely proportional to the square root of J_o. As shown in Fig. 52, the IS detector's detectivity is at least 1 order of magnitude lower than that of T2SL IB detectors. For most IS photodetectors, D^* is less than 3×10^7 cm Hz$^{1/2}$/W, while for IBs the values are above 1×10^8 cm Hz$^{1/2}$/W but in the MWIR region even exceed 1×10^9 cm Hz$^{1/2}$/W. This performance shows that bipolar devices based on the T2SL InAs/GaSb IB absorbers are good candidates for detectors operating near 300 K. Those IB QCPs combine the advantages of IB optical transitions with the excellent carrier-transport properties of the IB QCLs. The thermal generation rate at any temperature and λ_{cutoff} is usually orders of magnitude lower than that of the corresponding IS QCPs. This contributes to the fact that the operating temperature of IB QCPs is considerably higher than that of IS QCPs.

Figure 53 compares the estimated Johnson-noise-limited peak detectivities under zero bias (based on the measured R_oA product and responsivity) for QCPs with commercially available (Hg, Cd)Te photovoltaic detectors.

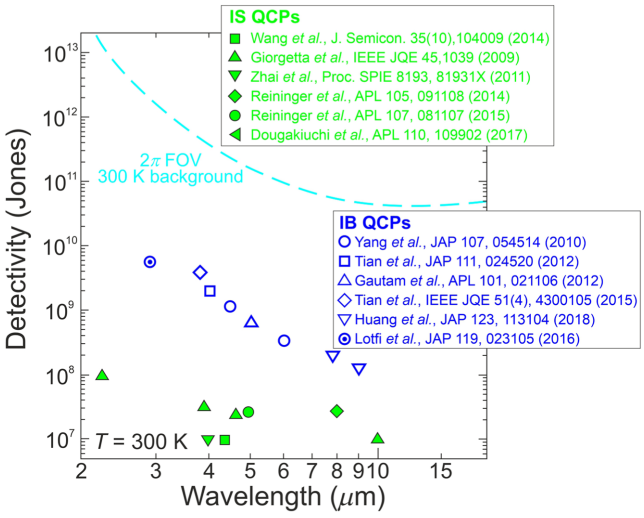

FIG. 52. Detectivity at room temperature versus wavelength for IS and IB QCPs (based on Ref. [54]).

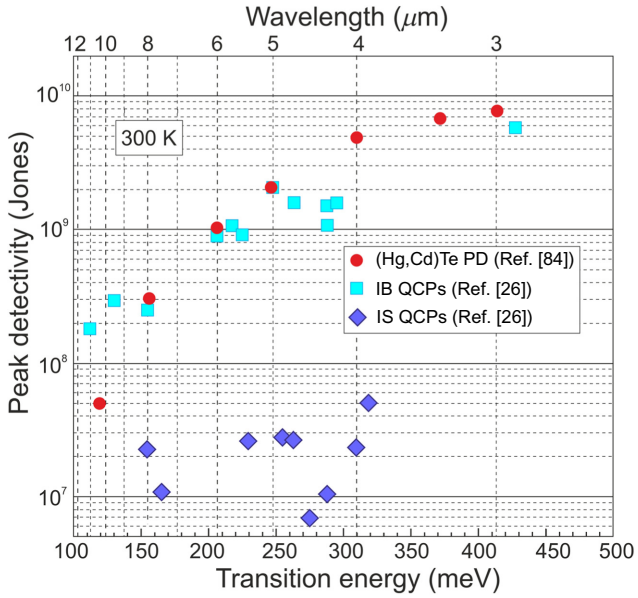

FIG. 53. Peak detectivity at room temperature versus transition energy and wavelength for commercially available (Hg, Cd)Te photodiodes (based on Ref. [84]) and IB and IS QCPs (based on Refs. [26,84]).

Due to intersubband transitions, the IS photodetectors are narrow-band devices. They are based on more mature material systems with well-established epitaxial growth and device-processing technologies. They are characterized by better uniformity and lower surface-leakage currents.

VIII. CONCLUSIONS AND OUTLOOK

IB QCPs have a complicated multilayer architecture and require sophisticated MBE growth procedures. Their design is particularly pronounced for high-temperature conditions and the LWIR range, where the carrier diffusion lengths are considerably reduced. Currently, their performance is comparable with that of (Hg, Cd)Te; however, due to strong covalent bonding of $A^{III}B^{V}$ semiconductors, QCPs can operate above room temperature, which is not reachable for the $A^{II}B^{VI}$ (Hg, Cd)Te counterpart. LWIR IB QCPs are capable of operating at temperatures as high as 340 K, while MWIR IB QCPs are reported to operate at 420 K.

It is expected that a better understanding of the quantum cascade device's physics and other aspects related to the design and material properties will enable improved high-performance HOT detectors. Flexibility in the structural design and material parameters provide remarkable room for improvement in device performance. Significant development and improvement are needed for the T2SL's carrier lifetime, where "Ga-free" exhibits potential in comparison with the InAs/GaSb system. Generally, $A^{III}B^{V}$ [to include

bulk (In, As)Sb and T2SLs] compounds exhibit inherently short SRH lifetimes, typically below 1 μs, requiring the barrier heterostructures to operate under HOT conditions. It must be stressed that (Hg, Cd)Te exhibits long SRH lifetimes, up to 50 ms, depending on λ_{cutoff}, and can operate with either architecture and may be diffusion or depletion-current limited. In addition, the advantages of T2SL InAs/(In, As)Sb over that of InAs/GaSb are related to better growth controllability and simpler manufacturability.

To compete with (Hg, Cd)Te, the IB QCPs based on T2SL InAs/(In, As)Sb active layers are predicted to be used with properly selected AlSb/(In, As)Sb, AlSb/InAs, and AlSb/GaSb barrier layers. Further improvement in detectivity can be reached by the growth of IB QCP structures on GaAs substrates for conversion into an immersion lens. The IB QCP's active elements (single pixel, with a size smaller than that of the operating wavelength to suppress thermal generation) connected with a dielectric resonator antenna should increase the performance under HOT conditions. The ultimate goal would be IB QCPs based on uncooled or minimally cooled FPAs.

The matched-absorber structure is reported to reach a higher performance in comparison with that of equal-absorber IB QCPs; however, the yield is not significant in relation to the use of the T2SL constituent materials for MBE growth. The IB QCPs are reported to reach the Rule 07 benchmark level of $10^{-3}/(\lambda_{\text{cutoff}}T) \sim 10^{-2}$–$10^{-3}$ A/cm^2.

From the IB QCP's equal-absorber performance, the detectivity can be increased by about 40%, assuming that the photoelectric gain contribution compensates for the quantum-efficiency decrease for the stages located distant from the very first absorber.

The discrete architecture of the QCP provides a great deal of flexibility for carrier-transport engineering to achieve high-speed operation, which determines the maximum bandwidth. The possibility of having them monolithically integrated with active components, for instance, lasers, offers avenues for telecommunication systems based on quantum devices [93]. The increasing availability of room-temperature QCLs, together with IR multistage photodetectors, should increase the number of applications.

After 60 years of research on (Hg, Cd)Te, a doping concentration below 5×10^{13} cm^{-3} has already been reached. This doping level is required to fabricate *P-i-N* heterostructures operating at room temperature in the LWIR spectral region with performance limited by background radiation. This fact provides further encouragement for achieving low-cost and high-performance MWIR and LWIR HOT (Hg, Cd)Te photodiodes. Under these circumstances and due to mature (Hg, Cd)Te technology, it will be rather difficult to compete with (Hg, Cd)Te photodiodes in the future. The main problem in the development of IB QCP technology is the challenge of their fabrication (complicated structure with many interfaces and strained thin layers) and high cost.

ACKNOWLEDGMENTS

This work is supported by the Polish National Science Centre within Projects No. 2018/31/B/ST7/01541 and No. 2018/30/M/ST7/00174.

[1] A. Rogalski, *Infrared and Terahertz Detectors* (CRC Press, Boca Raton, 2019).
[2] A. Rogalski, *2D Materials for Infrared and Terahertz Detectors* (CRC Press, Boca Raton, 2020).
[3] J. Piotrowski and A. Rogalski, Uncooled long wavelength infrared photon detectors, Infrared Phys. & Technol. **46**, 115 (2004).
[4] J. Piotrowski and A. Rogalski, *High-Operating-Temperature Infrared Photodetectors* (SPIE Press, Bellingham, 2007).
[5] J. Piotrowski and W. Gawron, Extension of longwavelength IR photovoltaic detector operation to near room-temperatures, Infrared Phys.& Technol. **36**, 1045 (1995).
[6] B. F. Levine, Quantum-well infrared photodetectors, J. Appl. Phys. **74**, R1 (1993).
[7] H. Schneider and H. C. Liu, *Quantum Well Infrared Photodetectors: Physics and Applications* (Springer, Berlin, 2007).
[8] D. Hofstetter, M. Beck, and J. Faist, Quantum-cascade-laser structures as photodetectors, Appl. Phys. Lett. **81**, 2683 (2002).
[9] L. Gendron, M. Carras, A. Huynh, V. Ortiz, C. Koeniguer, and V. Berger, Quantum cascade photodetector, Appl. Phys. Lett. **85**, 2824 (2004).
[10] J. C. Smith, L. C. Chiu, S. Margalit, A. Yariv, and A. Y. Cho, A new infrared detector using electron emission from multiple quantum wells, J. Vac. Sci. Technol. **B1**, 376 (1983).
[11] D. D. Coon and P. G. Karunasiri, New mode of IR detection using quantum wells, Appl. Phys. Lett. **45**, 649 (1984).
[12] L. C. West and S. J. Eglash, First observation of an extremely large-dipole infrared transition within the conduction band of a GaAs quantum well, Appl. Phys. Lett. **46**, 1156 (1985).
[13] B. F. Levine, K. K. Choi, C. G. Bethea, J. Walker, and R. J. Malik, New 10 μm infrared detector using intersubband absorption in resonant tunneling GaAlAs superlattices, Appl. Phys. Lett. **50**, 1092 (1987).
[14] H. Schneider, C. Schönbein, M. Walther, K. Schwarz, J. Fleissner, and P. Koidl, Photovoltaic quantum well infrared photodetectors: The four-zone scheme, Appl. Phys. Lett. **71**, 246 (1997).
[15] A. Gomez, M. Carras, A. Nedelcu, E. Costard, X. Marcadet, and V. Berger, Advantages of quantum cascade detectors, Proc. SPIE 6900, 69000J (2008).
[16] A. Buffaz, M. Carras, L. Doyennette, A. Nedelcu, P. Bois, and V. Berger, State of the art of quantum cascade photodetectors, Proc. SPIE 7660, 76603Q (2010).

[17] A. Buffaz, A. Gomez, M. Carras, L. Doyennette, and V. Berger, Role of subband occupancy on electronic transport in quantum cascade detectors, Phys. Rev. B **81**, 075304 (2010).

[18] A. Bigioli, G. Armaroli, A. Vasanelli, D. Gacemi, Y. Todorov, D. Palaferri, L. Li, A. G. Davies, E. H. Linfield, and C. Sirtori, Long-wavelength infrared photovoltaic heterodyne receivers using patch-antenna quantum cascade detectors, Appl. Phys. Lett. **116**, 161101 (2020).

[19] P. Krötz, D. Stupar, J. Krieg, G. Sonnabend, M. Sornig, F. Giorgetta, E. Baumann, M. Giovannini, N. Hoyler, D. Hofstetter, and R. Schieder, Applications for quantum cascade lasers and detectors in mid-infrared high resolution heterodyne astronomy, Appl. Phys. B **90**, 187 (2008).

[20] D. Hofstetter, F. R. Giorgetta, E. Baumann, Q. Yang, C. Manz, and K. Köhler, Mid-infrared quantum cascade detectors for applications in spectroscopy and pyrometry, Appl. Phys. B **100**, 313 (2010).

[21] F. R. Giorgetta, E. Baumann, M. Graf, Q. Yang, C. Manz, K. Köhler, H. E. Beere, D. A. Ritchie, E. Linfield, A. G. Davies, Y. Fedoryshyn, H. Jäckel, M. Fischer, J. Faist, and D. Hofstetter, Quantum cascade detectors, IEEE J. Quantum Electron. **45**, 1039 (2009).

[22] A. Delga, in *Mid-Infrared Optoelectronics. Materials, Devices, and Applications*, edited by E. Tournie, L. Cerutti (Elsevier, Duxford, 2020), pp. 337–377.

[23] R. Q. Yang, Infrared laser based on intersubband transitions in quantum wells, Superlattices Microstruct. **17**, 77 (1995).

[24] Y. Jiang, L. Li, R. Q. Yang, J. A. Gupta, G. C. Aers, E. Dupont, J. Baribeau, X. Wu, and M. B. Johnson, Type-I interband cascade lasers near 3.2 μm, Appl. Phys. Lett. **106**, 041117 (2015).

[25] R. Q. Yang, L. Li, L. Zhao, Y. Jiang, Z. Tian, H. Ye, R. T. Hinkey, C. Niu, T. D. Mishima, M. B. Santos, J. C. Keay, and M. B. Johnson, Recent progress in development of InAs-based interband cascade lasers, Proc. SPIE **8640**, 86400Q (2013).

[26] W. Huang, S. M. S. Rassela, L. Li, J. A. Massengale, R. Q. Yang, T. D. Mishima, and M. B. Santos, A unified figure of merit for interband and intersubband cascade devices, Infrared Phys. Technol. **96**, 298 (2019).

[27] D. Z. Garbuzov, H. Lee, V. Khalfin, R. Martinelli, J. C. Connolly, and G. L. Belenky, 2.3-2.7-(m room temperature CW operation of InGaAsSb-AlGaAsSb broad waveguide SCH-QW diode lasers, IEEE Photonics Technol. Lett. **11**, 794 (1999).

[28] J. G. Kim, L. Shterengas, R. U. Martinelli, G. L. Belenky, D. Z. Garbuzov, and W. K. Chan, Room-temperature 2.5 micron InGaAsSb/AlGaAsSb diode lasers emitting 1 W continuous waves, Appl. Phys. Lett. **81**, 3146 (2002).

[29] D. L. Partin, Lead salt quantum well diode lasers, Superlattices Microstruct. **1**, 131 (1985).

[30] Z. Shi, M. Tacke, A. Lambrecht, and H. Böttner, Midinfrared lead salt multi-quantum-well diode lasers with 282 K operation, Appl. Phys. Lett. **66**, 2537 (1995).

[31] R. Q. Yang, Z. Tian, J. F. Klem, T. D. Mishima, M. B. Santos, and M. B. Johnson, Interband cascade photovoltaic devices, Appl. Phys. Lett. **96**, 063504 (2010).

[32] W. Huang, *Thermophotovoltaic Devices and Infrared Photodetectors Based on Interband Cascade Structures* (University of Oklahoma, Norman, Oklahoma, 2020).

[33] M. A. Green, Do built-in fields improve solar cell performance?, Prog. Photovolt.: Res. Appl. **17**, 57 (2009).

[34] R. T. Hinkey and R. Q. Yang, Theory of multiple-stage interband photovoltaic devices and ultimate performance limit comparison of multiple-stage and single-stage interband infrared detectors, J. Appl. Phys. **114**, 104506 (2013).

[35] H. Lotfi, L. Lei, L. Li, R. Q. Yang, J. C. Keay, M. B. Johnson, Y. Qiu, D. Lubyshev, J. M. Fastenau, and A. W. K. Liu, High temperature operation of interband cascade infrared photodetectors with cutoff wavelengths near 8 μm, Opt. Eng. **54**, 063103 (2015).

[36] R. Q. Yang, W. Huang, L. Li, L. Lei, J. A. Massengale, T. D. Mishima, and M. B. Santos, Gain and resonant tunneling in interband cascade IR photodetectors, Proc. SPIE 10540, 105400E (2018).

[37] W. Huang, L. Li, L. Lei, J. A. Massengale, R. Q. Yang, T. D. Mishima, and M. B. Santos, Electric gain in interband cascade infrared photodetectors, J. Appl. Phys. **123**, 113104 (2018).

[38] R. Q. Yang, Z. Tian, Z. Cai, J. F. Klem, M. B. Johnson, and H. C. Liu, Interband-cascade infrared photodetectors with superlattice absorbers, J. Appl. Phys. **107**, 054514 (2010).

[39] A. Rogalski, M. Kopytko, and P. Martyniuk, *Antimonide-Based Infrared Detectors. A New Perspective* (SPIE Press, Bellingham, 2018).

[40] J. V. Li, R. Q. Yang, C. J. Hill, and S. L. Chung, Interbad cascade detectors with room temperature photovoltaic operation, Appl. Phys. Lett. **86**, 101102 (2005).

[41] Z. Tian, R. T. Hinkey, R. Q. Yang, D. Lubyshev, Y. Qiu, J. M. Fastenau, W. K. Liu, and M. B. Johnson, Interband cascade infrared photodetectors with enhanced electron barriers and p-type superlattice absorbers, J. Appl. Phys. **111**, 024510 (2012).

[42] N. Gautam, S. Myers, A. V. Barve, B. Klein, E. P. Smith, D. R. Rhiger, L. R. Dawson, and S. Krishna, High operating temperature interband cascade midwave infrared detector based on type-II InAs/GaSb strained layer superlattice, Appl. Phys. Lett. **101**, 021106 (2012).

[43] W. Pusz, A. Kowalewski, P. Martyniuk, W. Gawron, E. Plis, S. Krishna, and A. Rogalski, Mid-wavelength infrared type-II InAs/GaSb superllatice interband cascade photodetectors, Opt. Eng. **53**, 043107 (2014).

[44] Z.-B. Tian and S. Krishna, Mid-infrared interband cascade photodetectors with different absorber designs, IEEE J. Quant. Electron. **51**, 4300105 (2015).

[45] H. Lotfi, L. Lu, H. Ye, R. T. Hinkey, L. Lei, R. Q. Yang, J. C. Keay, T. D. Mishima, M. B. Santos, and M. B. Johnson, Interband cascade infrared photodetectors with long and very-long cutoff wavelengths, Infrared Phys. Technol. **70**, 162 (2015).

[46] L. Lei, L. Li, H. Ye, H. Lotfi, R. Q. Yang, M. B. Johnson, J. A. Massengale, T. D. Mishima, and M. B. Santos, Long wavelength interband cascade infrared photodetectors operating at high temperatures, J. Appl. Phys. **120**, 193102 (2016).

[47] L. Lei, L. Li, H. Lotfi, H. Ye, R. Q. Yang, T. D. Mishima, M. B. Santos, and M. B. Johnson, Midwavelength

interband cascade infrared photodetectors, Opt. Eng. **57**, 011006 (2018).

[48] K. Hackiewicz, J. Rutkowski, and P. Martyniuk, Optimal absorber thickness in interband cascade photodetectors, Infrared Phys. Technol. **95**, 136 (2018).

[49] K. Hackiewicz, J. Rutkowski, and P. Martyniuk, Long-wavelength interband cascade detector architectures for room temperature operation, IEEE J. Quantum Electron. **55**, 4000306 (2019).

[50] J. Piotrowski and A. Rogalski, Comment on "temperature limits on infrared detectivities of $InAs/In_xGa_{1-x}Sb$ superlattices and bulk $Hg_{1-x}Cd_xTe$" [*J. appl. phys*. **74**, 4774 (1993)], J. Appl. Phys. **80**, 2542 (1996).

[51] M. A. Kinch, *Fundamentals of Infrared Detectors* (SPIE Press, Bellingham, 2007).

[52] D. Z.-Y. Ting, A. Soibel, L. Höglund, J. Nguyen, C. J. Hill, A. Khoshakhlagh, and S. D. Gunapala, in *Semiconductors and Semimetals*, edited by S. D. Gunapala, D. R. Rhiger, C. Jagadish (Elsevier, Amsterdam, 2011), Vol. 84, pp.1–57.

[53] E. A. Plis, InAs/GaSb type-II superlattice detectors, Adv. Electron., 246769 (2014).

[54] A. Rogalski, P. Martyniuk, and M. Kopytko, Type-II superlattice photodetectors versus HgCdTe photodiodes, Prog. Quantum Electron. **68**, 100228 (2019).

[55] G. Ariyawansa, E. Steenbergen, L. J. Bissell, J. M. Duran, J. E. Scheihing, and M. T. Eismann, Absorption characteristics of mid-wave infrared type-II superlattices, Proc. SPIE **9070**, 90701J (2014).

[56] D. Z. Ting, A. Soibel, A. Khoshakhlagh, S. A. Keo, Sir B. Rafol, A. M. Fisher, B. J. Pepper, E. M. Luong, C. J. Hill, and S. D. Gunapala, Advances in III-V semiconductor infrared absorbers and detectors, Infrared Phys. Technol. **97**, 210 (2019).

[57] D. Z. Ting, A. Soibel, and S. D. Gunapala, Type-II superlattice hole effective masses, Infrared Phys. Technol. **84**, 102 (2017).

[58] J. Chu, B. Li, K. Liu, and D. Tang, Empirical rule of intrinsic absorption spectroscopy in $Hg_{1-x}Cd_xTe$, J. Appl. Phys. **75**, 1234 (1994).

[59] E. J. Johnson, in *Semiconductors and Semimetals*, edited by K. Willardson, A. C. Beer (Academic Press, New York, 1967), Vol. 3, pp.153–258.

[60] P. T. Webster, N. A. Riordan, S. Liu, E. H. Steenbergen, R. A. Synowicki, Y.-H. Zhang, and S. R. Johnson, Measurement of InAsSb bandgap energy and InAs/InAsSb band edge positions using spectroscopic ellipsometry and photoluminescence spectroscopy, J. Appl. Phys. **118**, 245706 (2015).

[61] P. T. Webster, N. A. Riordan, S. Liu, E. H. Steenbergen, R. A. Synowicki, Y.-H. Zhang, and S. R. Johnson, Absorption properties of type-II InAs/InAsSb superlattices measured by spectroscopic ellipsometry, Appl. Phys. Lett. **106**, 061907 (2015).

[62] P. C. Klipstein, Y. Livneh, A. Glozman, S. Grossman, O. Klin, N. Snapi, and E. Weiss, Modeling InAs/GaSb and InAs/InAsSb superlattice infrared detectors, J. Electron. Mater. **43**, 2984 (2014).

[63] I. Vurgaftman, G. Belenky, Y. Lin, D. Donetsky, L. Shterengas, G. Kipshidze, W. L. Sarney, and S. P. Svensson, Interband absorption strength in long-wave infrared type-II superlattices with small and large superlattice periods compared to bulk materials, Appl. Phys. Lett. **108**, 222101 (2016).

[64] E. H. Steenbergen, B. C. Connelly, G. D. Metcalfe, H. Shen, M. Wraback, D. Lubyshev, Y. Qiu, J. M. Fastenau, A. W. K. Liu, S. Elhamri, O. O. Cellek, and Y.-H. Zhang, Significantly improved minority carrier lifetime observed in a long-wavelength infrared III-V type-II superlattice comprised of InAs/InAsSb, Appl. Phys. Lett. **99**, 251110 (2011).

[65] E. H. Steenbergen, in *Mid-Infrared Optoelectronics. Materials, Devices, and Applications*, edited by E. Tournie, L. Cerutti (Elsevier, Duxford, 2020), pp. 415–453.

[66] W. Huang, L. Li, L. Lei, J. A. Massengale, H. Ye, R. Q. Yang, T. D. Mishima, and M. B. Santos, Minority carrier lifetime in mid-wavelength interband cascade infrared photodetectors, Appl. Phys. Lett. **112**, 251107 (2018).

[67] B. C. Connelly, G. D. Metcalfe, H. Shen, and M. Wraback, Direct minority carrier lifetime measurements and recombination mechanism in long-wave infrared type-II superlattices using time-resolved photoluminescence, Appl. Phys. Lett. **97**, 251117 (2010).

[68] D. Wang, D. Donetsky, S. Jung, and G. Belenky, Carrier lifetime measurements in long-wave infrared InAs/GaSb superlattices under low excitation conditions, J. Electron. Mater. **41**, 3027 (2012).

[69] M. Delmas, J. B. Rodriguez, and P. Christol, Electric modeling of InAs/GaSb superlattice mid-wavelength infrared PIN photodiode to analyze experimental dark current characteristics, J. Appl. Phys. **116**, 113101 (2014).

[70] R. K. Ahrenkiel, in *Semiconductors and Semimetals*, edited by R. K. Ahrenkiel, M. S. Lundstrom (Academic Press, New York, 1993), Vol. 39, pp.39–150.

[71] A. Y. Cho and J. R. Arthur, Molecular beam epitaxy, Prog. Solid State Chem. **10**, 157 (1975).

[72] M. A. Herman and H. Sitter, *Molecular Beam Epitaxy: Fundamentals and Current Status* (Springer, Berlin, 2012).

[73] H. Ye, H. Lotfi, L. Li, R. T. Hinkey, R. Q. Yang, L. Lei, J. C. Keay, M. B. Johnson, T. D. Mıshıma, and M. B. Santos, Multi-stage interband cascade photovoltaic devices with a bandgap of 0.23 eV operating above room temperature, Chin. Sci. Bull. **59**, 950 (2014).

[74] D. Z. Ting, A. Soibel, A. Khoshakhlagh, Sir B. Rafol, S. A. Keo, L. Höglund, A. M. Fisher, E. M. Luong, and S. D. Gunapala, Mid-wavelength high operating temperature barrier infrared detector and focal plane array, Appl. Phys. Lett. **113**, 021101 (2018).

[75] D. Wu, J. Li, A. Dehzangi, and M. Razeghi, Mid-wavelength infrared high operating temperature pBn photodetectors based on type-II InAs/InAsSb superlattice, AIP Adv. **10**, 025018 (2020).

[76] P. C. Klipstein, E. Avnon, Y. Benny, R. Fraenkel, A. Glozman, S. Grossman, O. Klin, L. Langoff, Y. Livneh, I. Lukomsky, M. Nitzani, L. Shkedy, I. Shtrichman, N. Snapi, A. Tuito, and E. Weiss, InAs/GaSb type II superlattice barrier devices with a low dark current and a high quantum efficiency, Proc. SPIE **9070**, 90700U (2014).

[77] D. Z.-Y. Ting, C. J. Hill, A. Soibel, S. A. Keo, J. M. Mumolo, J. Nguyen, and S. D. Gunapala, A high-performance long wavelength superlattice complementary barrier infrared detector, Appl. Phys. Lett. **95**, 023508 (2009).

[78] B.-M. Nguyen, D. Hoffman, P.-Y. Delaunay, and M. Razeghi, Dark current suppression in type II InAs/GaSb superlattice long wavelength infrared photodiodes with M-structure barrier, Appl. Phys. Lett. **91**, 163511 (2007).

[79] H. Ye, L. Li, H. Lotfi, L. Lei, R. Q. Yang, J. C. Keay, T. D. Mishima, M. B. Santos, and M. B. Johnson, Molecular beam epitaxy of interband cascade structures with InAs/GaSb superlattice absorbers for long-wavelength infrared detection, Semicond. Sci. Technol. **30**, 105029 (2015).

[80] D. Zuo, P. Qiao, D. Wasserman, and S. L. Chuang, Direct observation of minority carrier lifetime improvement in InAs/GaSb type-II superlattice photodiodes via interfacial layer control, Appl. Phys. Lett. **102**, 141107 (2013).

[81] W. E. Tennant, D. Lee, M. Zandian, E. Piquette, and M. Carmody, Mbe HgCdTe technology: A very general solution to IR detection, described by 'Rule 07', a very convenient heuristic, J. Electron. Mater. **37**, 1406 (2008).

[82] Z.-B. Tian, S. E. Godoy, H. S. Kim, T. Schuler-Sandy, J. A. Montoya, and S. Krishna, High operating temperature interband cascade focal plane arrays, Appl. Phys. Lett. **105**, 051109 (2014).

[83] W. Huang, L. Lei, L. Li, J. A. Massengale, R. Q. Yang, T. D. Mishima, and M. B. Santos, Current-matching versus non-current-matching in long wavelength interband cascade infrared photodetectors, J. Appl. Phys. **122**, 083102 (2017).

[84] https://vigo.com.pl/wp-content/uploads/2017/06/VIGO-Catalogue.pdf

[85] L. Lei, L. Li, W. Huang, J. A. Massengale, H. Ye, H. Lotfi, R. Q. Yang, D. Tetsuya, M. B. Santos, and M. B. Johnson, Resonant tunneling and multiple negative differential conductance features in long wavelength interband cascade infrared photodetectors, Appl. Phys. Lett. **111**, 113504 (2017).

[86] D. Lee, P. Dreiske, J. Ellsworth, R. Cottier, A. Chen, S. Tallarico, A. Yulius, M. Carmody, E. Piquette, M. Zandian, and S. Douglas, in *Extended Abstracts. The 2019 U.S. Workshop on the Physics and Chemistry of II-VI Materials* (2019), pp. 13–15.

[87] D. Lee, P. Dreiske, J. Ellsworth, R. Cottier, A. Chen, S. Tallaricao, A. Yulius, M. Carmody, E. Piquette, M. Zandian, and S. Douglas, Law 19 - the ultimate photodiode performance metric, Proc. SPIE 11407, 114070X (2020).

[88] M. A. Kinch, *State-of-the-Art Infrared Detector Technology* (SPIE Press, Bellingham, 2014).

[89] D. Lee, M. Carmody, E. Piquette, P. Dreiske, A. Chen, A. Yulius, D. Edwall, S. Bhargava, M. Zandian, and W. E. Tennant, High-operating temperature HgCdTe: A vision for the near future, J. Electron. Mater. **45**, 4587 (2016).

[90] D. R. Rhiger, Performance comparison of long-wavelength infrared type II superlattice devices with HgCdTe, J. Electron. Mater. **40**, 1815 (2011).

[91] P. C. Klipstein, E. Avnon, D. Azulai, Y. Benny, R. Fraenkel, A. Glozman, E. Hojman, O. Klin, L. Krasovitsky, L. Langof, I. Lukomsky, M. Nitzani, I. Shtrichman, N. Rappaport, N. Snapi, E. Weiss, and A. Tuito, Type II superlattice technology for LWIR detectors, Proc. SPIE **9819**, 98190T (2016).

[92] A. Rogalski and R. Ciupa, Performance limitation of short wavelength infrared InGaAs and HgCdTe photodiodes, J. Electron. Mater. **28**, 630 (1999).

[93] H. Lotfi, L. Li, S. M. Shazzad Rassel, R. Q. Yang, C. J. Corrége, M. B. Johnson, P. R. Larson, and J. A. Gupta, Monolithically integrated mid-IR interband cascade laser and photodetector operating at room temperature, Appl. Phys. Lett. **109**, 151111 (2016).